Neuromorphic Imaging Cytometry

Ziyao Zhang

Principal Supervisor
Prof. Omid Kavehei

Auxiliary Supervisors
Dr. Daniele Vigolo, Dr. Helen M. McGuire

A thesis submitted in fulfillment
of the requirements of the degree of
Doctor of Philosophy

Faculty of Engineering
School of Biomedical Engineering
The University of Sydney

February 2025

Declaration

I hereby declare that this submission is my original work and, to the best of my knowledge and belief, contains no material previously published or authored by another individual, nor any content that has been substantially used to obtain another degree or diploma from this university or any other institution of higher learning, except where duly acknowledged in the text.

Ziyao Zhang

22 February 2025

Abstract

Imaging Flow Cytometry (IFC) is an indispensable cell-analytic tool that provides multi-parametric measurements with high-dimensional feedback derived from single-cell images. It enables profound insights into cell signalling, co-localisation, cell-to-cell interaction and Deoxyribonucleic Acid (DNA) studies. However, the traditional Frame-Based Sensor (FBS) adopted IFC can inhibit its performance, bound by the triangle of imaging constraints: speed, resolution and sensitivity; increasing one parameter can lead to degradation in others. This trade-off correlation has fundamentally hindered the development and generalisation of IFC. Considering the size of a cell population, a significant data volume can be generated during analysis, which can be cumbersome to operate and analyse for real-time applications. In addition, the rich spatial information acquired IFC has exceptional uses with Machine Learning (ML) models to automate cell analysis, gating and revealing rare cell events.

Herein, we introduced a Neuromorphic Imaging Cytometry (NIC) to characterise cells with superior temporal resolution, data efficiency and fluorescence sensitivity. Taking the advantages of data sparsity in neuromorphic vision, the proposed platform and curated dataset were combined with hybrid Spiking Neural Networks (SNN) models to perform cell classification and enable in-depth analysis with human blood cells, immortal cell lines and artificial particles. To the best of our knowledge, our research enabled the first novelty of neuromorphic-enabled cytometry applications. This dissertation encompassed the entire research milestones including the initial conceptualisation of NIC with artificial particles; implementation of fundamental cytometric functions; object detection with biological cells; advanced ML cell analysis by lightweight model on convoluted cell classes and morphologies. Combining the data sparsity in neuromorphic imaging with a lightweight hybrid SNN model and operation platform, this paradigm can become a fundamental backbone for next-generation, ML-driven cytometry.

Acknowledgements

First and foremost, I would like to thank my supervisors, Professor Omid Kavehei, Dr Daniele Vigolo and Dr Helen McGuire for generously providing their expertise, guidance, and support in consolidating this interdisciplinary research. Their mentorship has been instrumental in shaping my academic milestones and ensuring the success of this work.

I would like to thank Dr Jason K. Eshraghian from the Department of Electrical and Computer Engineering at the University of California Santa Cruz, for sharing his profound expertise in machine learning and neuromorphic architectures. I would like to thank Professor Ken Tye Yong for his professional consultation in microfluidics.

I would like to acknowledge the Faculty of Biomedical Engineering and the University of Sydney for their financial support through the Postgraduate Research Support Scheme (PRSS) grants. I am equally grateful to the Charles Perkins Centre for their invaluable assistance in biological sample collection and preparation, which provided a solid foundation for the experimental aspects of this research.

This research was supported by an Australian Government Research Training Program (RTP) Scholarship.

Lastly and most importantly, I would like to express my sincere gratitude to my partner, parents and family for their unconditional love, patience and support. They are the most crucial key to my success in this work.

Contents

List of Figures

List of Tables

Nomenclature

List of Acronyms

Instrumentation and Methodology

AT	Accumulation Time
BSI	Back-Side Illuminated
CCD	Charged-Coupled Devices
CMOS	Complementary Metal-Oxide-Semiconductor
CPU	Central Processing Unit
DEP	Dielectrophoretic
DR	Dynamic Range
EVK3	Evaluation Kit 3
EVK4	Evaluation Kit 4
EVS	Event Vision Sensor
FBS	Frame-Based Sensor
FC	Flow Cytometry
FITC	Fluorescein Isothiocyanate
FPGA	Field-Programmable Gate Array
fps	Frames Per Second
FSC	Forward Scatter
GPU	Graphics Processing Unit
HDR	High Dynamic Range
ICS	Image-based Cell Sorting
IFC	Imaging Flow Cytometry
MAC	Multiply-Accumulate
NIC	Neuromorphic Imaging Cytometry
NVS	Neuromorphic Vision Sensor
PDMS	Polydimethylsiloxane
PMMA	Polymethyl Methacrylate
PMTs	PhotoMultiplier Tubes
PS	Polystyrene
RAM	Random Access Memory
sCMOS	Scientific Complementary Metal-Oxide-Semiconductor

SSC	Side Scatter
VRAM	Video Random Access Memory

Machine Learning Architecture and Analysis

2D	Two-Dimensional
3D	Three-Dimensional
AI	Artificial Intelligence
AUC	Area Under the Curve
BNTT	Batch Normalisation Through Time
CBAM	Convolutional Block Attention Module
CBAM-SNN	Block Attention Module with Spiking Neural Network
CNN	Convolutional Neural Network
CSNN	Convolutional Spiking Neural Networks
DL	Deep Learning
EMS	Energy-efficient Membrane-Shortcut
EMS-ResNet	Energy-efficient Membrane-Shortcut Residual Network
EMS-YOLO	Energy-efficient Membrane-Shortcut You Only Look Once
FNN	Feedforward Neural Network
LCB	Layer-Connected Block
LIF	Leaky Integrate-and-Fire
LSTM	Long Short-Term Memory
mAP	Mean Average Precision
ML	Machine Learning
MS	Membrane-Shortcut
PCA	Principal Component Analysis
ResNet	Residual Network
RNN	Recurrent Neural Network
SNN	Spiking Neural Networks
SNN-YOLO	Spiking YOLO
UMAP	Uniform Manifold Approximation and Projection
YOLO	You Only Look Once
YOLOv3	You Only Look Once version 3

Biological and Chemical Sample

BSA	Bovine Serum Albumin
DMEM	Dulbecco's Modified Eagle's Medium
DNA	Deoxyribonucleic Acid
EDTA	Ethylenediaminetetraacetic Acid
HUVECs	Human Umbilical Vein Endothelial Cells
MCF-7	Michigan Cancer Foundation-7
PBS	Phosphate-Buffered Saline
RBCs	Red Blood Cells

Chapter 1

Introduction

1.1 Background

1.1.1 Flow cytometry

Flow Cytometry (FC) is a powerful cell analytic tool that provides multiparametric readouts of cells in a high-throughput manner. It enables cells to be analysed in large quantities, extracting phenotypical and fluorescence-mediated features for characterisation (Adan et al., 2017; McKinnon, 2018). Traditional FC contains three core systems: the fluidics system drives samples forward and induces hydrodynamic focusing via sheath fluid (commonly a buffered saline solution) with the sample stream enclosed at the centre. This action aligns cells laminar and single-file through a laser interrogation point for cell measurement. The optic system adopts lasers as an excitation source, measuring the light scattering and fluorescence signals emitted from the samples. Collections optics commonly use PhotoMultiplier Tubes (PMTs) or photodiodes to detect light signals. The electronic system converts the signals into electrical pulses for digital readouts, which can be visualised as plots or histograms (Adan et al., 2017; McKinnon, 2018; Shapiro and Telford, 2009; Wilkerson, 2012). In FC, FSC and SSC are essential parameters that indicate varied features of the cells.FSC detects light diffraction in a forward direction, along the same path as the laser, indicating the size or surface area of the cells. SSC measures the scattering light at a 90-degree angle to the laser, representing the granularity or internal complexity of the cells (Cossarizza et al., 2019; Reggeti and Bienzle, 2011). Such a paradigm allows cells to be screened in a high-throughput manner with multiparametric analysis, allowing a sampling rate of more than 10,000 cells/s (McKinnon, 2018; Rees et al., 2022). FC has enabled profound applications in multiple disciplines, including immunology, virology, molecular biology, cancer biology and infectious disease monitoring (McKinnon, 2018). However, this robust device describes cells based on pulse profiles without providing any direct vision of the samples, limiting the interpretation and high-dimensional features of the cell data.

1.1.2 Imaging flow cytometry

IFC combines the working principles of FC and fluorescence microscopy to characterise cells with high-dimensional parameters derived from single-cell images (Barteneva et al., 2012; Rees et al., 2022). It reveals high-dimensional resolutions of the samples such as cell area, morphology, texture and marker localisation, which are particularly useful for applications in cell signalling, cell-to-cell interactions, DNA repair and co-localisation studies (Gorecki et al., 2025; Grimwade et al., 2017; McKinnon, 2018; Rožanc et al., 2021). Furthermore, the differences in cell morphology, structure and composition are closely linked to their physiological function and are crucial for cell identity (Caicedo et al., 2017; Nitta et al., 2018). For instance, cell geometry affects intracellular signalling and is critical in regulating cell growth and differentiation (Aragona et al., 2013; Chen et al., 1997; Kilian et al., 2010; von Erlach et al., 2018). The localisation of transcription factors to the nucleus and cytoplasm can result in drastic differences in cell behaviour (Cai et al., 2008; Görner et al., 1998; Hao et al., 2013). Also, the morphological information of cells has been adopted as the gold standard for disease diagnosis and prognosis (Salek et al., 2023; Salto-Tellez, 2018). A range of other morphological characteristics are likely connected to unique cellular functions (Boutros et al., 2015; Mackinder et al., 2017; Moor et al., 2017; Nitta et al., 2018; Pernas et al., 2018; Zenker et al., 2017). IFC operates in a similar paradigm as FC with an image of each cell available, typically captured by Charged-Coupled Devices (CCD) or CMOS sensors (Han et al., 2016; LaBelle et al., 2021; Rees et al., 2022). Despite the rich spatial information collected, like any image-enabled system, IFC is also bound to the triangle of imaging constraints: speed, resolution and sensitivity; elevating one performance can render degradation in others (Rees et al., 2022). Therefore, Numerous efforts have been implemented to overcome this trade-off. The commercialised IFC ImageStream system (Luminex) utilises a time delay integration approach with CCD cameras to enhance the resolution at high speed by synchronously stacking pixel information row by row across the sensors, providing an improved throughput of up to 5,000 cells/s at 20 × magnification and traditional IFC operates between 2,000 and 3,000 cells/s at 20 × magnification (Basiji et al., 2007; Holzner et al., 2021). While these strategies are effective, IFC still has more than one order of magnitude lower than non-imaging flow cytometers owing to the data-expensive image acquisition mechanism (Holzner et al., 2021). A comprehensive review on IFC by Rees et al. (2022) states that the current device has limitations on measuring repeated time-lapse imaging of the same target and Three-Dimensional (3D) resolution. Objects can only be captured once as they pass through the imager, limiting the feedback to a single snapshot of the cells and suitability for tomographic flow cytometry, where it furnishes complete characterisations in 3D (Merola et al., 2017; Mertz, 2011). Sorting is also an essential functionality of a cytometric system to perform physical isolation of particular cell types, allowing downstream analysis of the target cells. A major modernisation in high-speed image sensing and intelligent data analysis is required to achieve the sorting capability (Rees et al., 2022). Moreover, the frame-based architecture in IFC can register enormous pixel data of blank and redundant background information irrelevant to cell events. This can render a significant data volume and is expensive for real-time low-latency tasks. Especially considering the concentration of a cell population can be easily over 1×10^6 cells/mL and multiple tests can be required for one experiment. With the ImageStream system, a sample concentration of $2–3 \times 10^7$ cells/mL is recommended for operation (Rees et al., 2022). Thus, a promising sensing method to resolve the conventional challenges in IFC should include (1) high temporal resolution for fast detection to elevate the throughput and repeated time-lapse imaging for enriched characterisation. (2) data efficiency for real-time cell analysis and decision-making to implement sorting capability.

1.1.3 Mannual gating for cytometric data

Manual gating is an analytic technique adopted with cytometric data to characterise cell phenotypes utilising several 2D scatter plots based on morphological-related parameters and assigned fluorescence signals (Lippeveld et al., 2019). A polynomial region is defined to gate out the population of interest, which allows the target cells or cell components to be analysed from a mixture. Manual gating can effectively isolate populations of interest but introduces several challenges, particularly with high-dimensional cytometry data. (1) Gating relies on an experienced researcher or expert to perform and interpret morphological and fluorescence data accurately. (2) This expert-dependent process may need to be repeated depending on the variability of the experiment and samples, creating a heavy workload for large-scale studies (Saeys et al., 2016). (3) Manual gating of the high-dimensional cytometry data can inhibit the interpretation into a bivariate hierarchical analysis of 2D scatter plots. In contrast, IFC is designed to provide multivariate spatial feedback, revealing more complex and insightful data structures. (4) The process is also prone to subjective bias and can be challenging to reproduce. (5) Using multiple fluorescence stains for cell readout and gating can be expensive, introduce confounding effects, and slow the workflow (Chen et al., 1993; Miltenburger et al., 1987; Wojcik and Dobrucki, 2008). A stain-free approach has drawn attention in bio-imaging in the last decades (De Wit et al., 2015; Freudiger et al., 2008; Wang et al., 2010).

Therefore, an automated gating approach with label-free samples is crucial to overcome these drawbacks, optimising the IFC workflow, analysis and expense. Numerous efforts have been implemented to annotate cell populations using ML models and uncover rare cell events from high-dimensional data (Arvaniti and Claassen, 2017; Cheng et al., 2022; Hu et al., 2022, 2020; Qiu et al., 2011).

1.2 Towards next-generation AI-assisted imaging cytometry

1.2.1 Neuromorphic vision sensor

NVS, also known as the event camera or event-based vision sensor, dynamic vision sensor or silicon retina, is a bio-inspired photosensor that imitates the neural architecture of the biological eye (Gallego et al., 2020; Howell et al., 2020; Lichtsteiner et al., 2008; Takatsuka et al., 2024). In the visual system, the receptors on the retina convert light into visual signals for transmission to the brain. Neurons process the light and dark conditions from the signals, and retinal ganglion cells then send this information to the brain's visual cortex for interpretation (Takatsuka et al., 2024). NVS resembles the transient pathways up to retinal ganglion cells (Gallego et al., 2020). Compared to traditional FBS, which captures images at a fixed frame rate, NVS detects brightness changes in a scene and transmits only the activated array address via the asynchronous firing pixels. In detail, each pixel registers a polarity output (+/-) depending on the brightness changes, where an increase in brightness is recorded as a positive (+) change; a decrease is registered as a negative (-) change; when there are no changes presented, the pixel remains inactivated for recording, meaning no events are transmitted and output by the sensor. With the address-event, which encodes the (x, y) address of pixel in the array, polarity (p) and timestamps (t) of events, NVS outputs an event data stream can be considered as a sequence of (x, y, p, t). This unique event-driven perception enables superior data efficiency, spatiotemporal resolution (in the scale of μs) and dynamic range (>120 dB versus 60 dB) with low power consumption compared to conventional FBS (Gallego et al., 2020; Lichtsteiner et al., 2008; Mueggler et al., 2017) The specification of the NVS compared to the FBSs adopted in cell imaging, sorting and monitoring were illustrated in Table 1.1.

Table 1.1 – Comparison of EVK4 to frame-based cameras utilised for cell imaging, sorting and monitoring. An equivalent frame rate of EVK4 was reported for comparative reference.

	NVS	**Traditional FBSs**			
	Current work	Nawaz et al. (2023, 2020)	Lee et al. (2021)	Isozaki et al. (2020b)	Takatsuka et al. (2024)
Vision Sensor	EVK4 (IMX636)	EoSens CL (MC1362)	DMK 37AUX287	Phantom v2640	FASTCAM Nova S6
Resolution (pixels)	1280×720	1280×1024	720×540	1024×976	1024×768
Frame Rate (fps)	$> 10,000$	500	539	$9,440$	9000
Pixel Size (μm)	4.86	14	6.9	13.5	20
Dynamic Range (dB)	> 120	60	60	64.1	72.2
Power usage (W)	$0.5 \sim 1.5$	7	1.7	280	138
Output	events	frames	frames	frames	frames

1.2.2 Neuromorphic imaging cytometry

Considering the everlasting trade-off challenges in IFC, NVS can be a suitable alternative to resolve them or enhance the existing capabilities with the advantages as follows: (1) NVS has a high temporal resolution equivalent to over 10,000 Frames Per Second (fps), which is suitable for detecting objects in high velocity, avoiding motion-induced artefact and degradation. (2) the High Dynamic Range (HDR) (> 120 dB) can detect fluorescence signals effectively. Fluorescence probes are crucial for characterising a living cell's proteins, enzymes and biomolecules. Many of these molecules exist in trace amounts or fluctuate, leading to absence or poor visualisation (Hirano et al., 2022; Izumi et al., 2009; Li et al., 2023; Nagai et al., 2004; Vinegoni et al., 2018, 2016). Although increasing the excitation power is the most robust strategy to elevate fluorescent photons, extensive research has demonstrated that overexposure to light sources can cause phototoxicity, photobleaching and tissue heating on cells (Hoebe et al., 2007; Icha et al., 2017; Laissue et al., 2017; Li et al., 2023; Podgorski and Ranganathan, 2016; Skylaki et al., 2016). Thus, a detection system with HDR is critical to maintain a sustainable enriched and in-depth analysis of cells and targeted molecules. Our work, Zhang et al. (2024a) has proved the superior fluorescence sensitivity of NVS compared to a traditional CMOS camera when observing Fluorescein Isothiocyanate (FITC) particles with low photon budget. (3) owing to sparse activation in event-based perception, NVS can report an efficient pixel collection that only focuses on cell phenotype instead of shuttering all pixels in a sensor for full-frame readout at a fixed time interval. Characterising cells with frame-based architecture can accumulate enormous pixel data registered with blank and redundant background information irrelevant to cell events. Such data structures can generate a significant data volume and are cumbersome for real-time processing. (4) portability, NVS can be portable to achieve high performance. Our experiment equipped an EVK4 camera with the dimensions of $30 \times 30 \times 36$ mm^3 ($W \times H \times D$). This can enable ease of use and simplicity of integration. (5) cost, for FBS to achieve a frame rate over 10,000 fps, a professionally graded high-speed camera system is required, which can be an overbearing cost for research and start-up projects. A cost and respective frame rate comparison of EVK4 to other FBSs were illustrated in Fig. 1.1. The schematic of the proposed NIC platform is illustrated in Fig. 1.2.

Our publication, Zhang et al. (2022) introduced the first novelty and conceptualisation of NIC by integrating an NVS with a microfluidic platform to observe Polystyrene (PS)-based microparticles. This experiment simulated the fluidics and sample conditions in IFC, demonstrating that NVS can deliver a desired resolution when registering microscale targets at a relatively high speed. Recently, numerous endeavours have been implemented to develop NIC with varied modalities and ML approaches. The research conducted by Abreu et al. (2023) utilised neuromorphic hardware and SNN for rapid and energy-efficient computation to solve a binary particle classification task for 16 μm and 20 μ Polymethyl Methacrylate (PMMA) microspheres. The proposed network achieved 98.5% accuracy with the event-based pipeline and 97.5% on frame data. The following work of Gouda et al. (2024b) utilised a surrogate gradient method instead of the previous logistic regression, accomplishing a 99% accuracy for particles with diameters of 9, 12, 16 and 20 μm. Recent investigation by Gouda et al. (2024a) on fungal cells and PMMA microparticle classification with unsupervised and supervised Learning using K-means, Principal Component Analysis (PCA), and Logistic Regression, accomplishing a 100% accuracy with PCA method without relying on training annotations. Furthermore, the research conducted

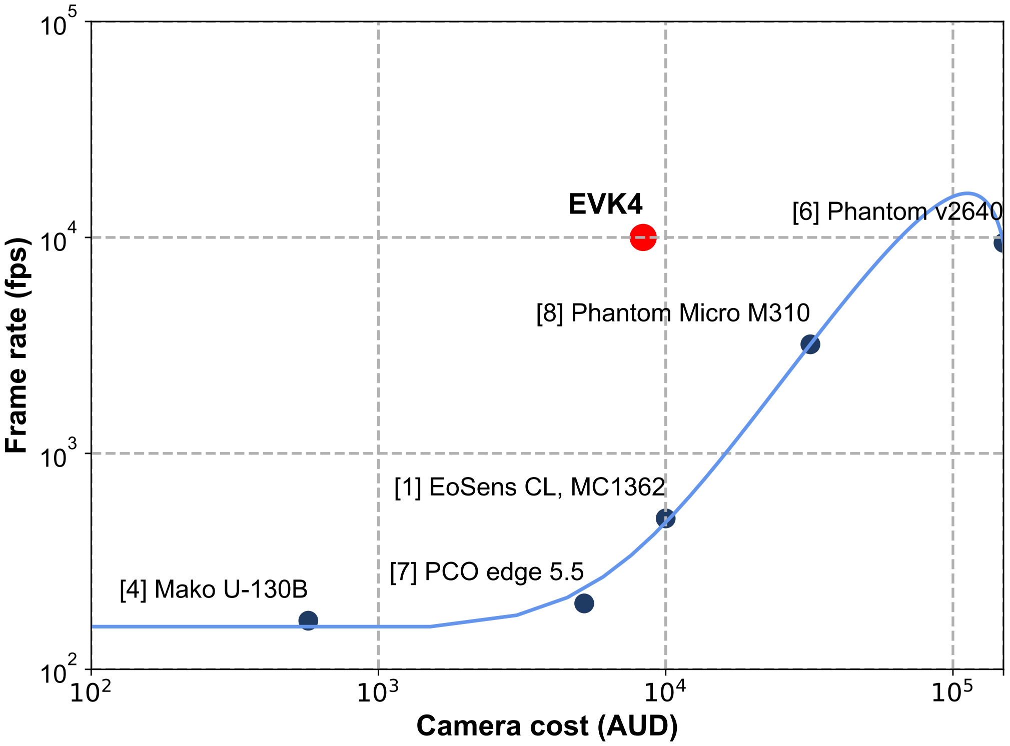

Figure 1.1 – The imaging cameras applied to different image-based cell sorting systems and their relevant framerate at full resolution. The camera cost is in Australian Dollars (AUD). The cameras used in the systems are shown on the graph: Mako U-130B, Allied Vision Technologies, Germany (Sesen and Whyte, 2020); PCO edge 5.5, PCO Imaging, Germany (Isozaki et al., 2020a); EVK4, Prophesee, France; EoSens CL, MC1362, Mikrotron, Germany (Nawaz et al., 2020); Phantom Miro M310 (Sciambi and Abate, 2015), Phantom v2640, Vision Research, USA (Isozaki et al., 2020a).

by Tsirigotis et al. (2023) combined NVS with a convolutional photonic accelerator based on an optical spectrum slicing for PMMA particle classification, resulting in a record of 2,988 images per particle. The following investigation, Tsilikas et al. (2023) employed lightweight ML schemes, reporting a 97.6% accuracy at a speed of 0.8 m/s. The recent work conducted by Tsilikas et al. (2024) developed NIC integrated with lightweight photonic neuromorphic processing to accomplish high classification accuracy for PMMA particles of 12 μm, 16 μm and 20 μm with a massive reduction in trainable parameters of the network. The proposed architecture reported a classification accuracy of 98.2% and 98.6% for the optimal Feedforward Neural Network (FNN)

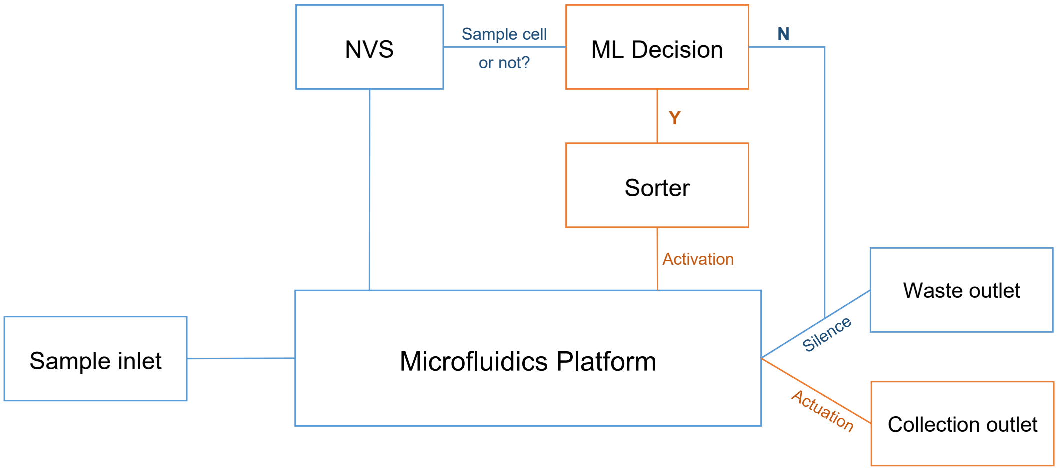

Figure 1.2 – The proposed schematic of NIC platform. Cells will be introduced to the channel via a syringe or a fluidic canal. Once the field of view of NVS detects the cells, a decision will be resulted based on the particles. If positive, a signal will be sent to activate the sorter, providing actuation to the cell pathway and deviating it into the collection outlet. If negative, the sorter will remain silent, and the cell will stay in the same pathway for the waste outlet.

and Recurrent Neural Network (RNN) configurations. Another prominent study published recently by (He et al., 2024) developed a neuromorphic-enabled cell sorter to perform binary classification of normal RBCs and spherocytes, achieving an average error of 0.99

To expand the research on NIC, in Zhang et al. (2023), we implemented the functions of object counting and size estimation in NIC and compared the performance to a conventional FC, CytoFlex as the baseline. We achieved comparable results for 8 μ m and 15 μ m particles and THP-1 cells (a human monocytic leukaemia cell line), demonstrating that NIC can achieve the desired accuracy and functionality of an FC with the cell resolution provided by the latter. This work also concludes one of the key innovations and advantages of NVS for providing superior fluorescence sensitivity by showing a prominent display of FITC-marked microparticles at low excitation, where conventional CMOS can not deliver any visual feedback at the excitation level. Our continuous work on cell detection using a convolutional SNN achieved an average class accuracy of 97.4% for 3 μm, 8 μm, 15 μm particles, THP-1 and LL/2 cells (a lewis lung carcinoma cell line). This result indicates that a ML approach can be adapted to automate the gating and analysis process for data-rich cell research. Last and most importantly, most of this domain is currently limited to experimenting with artificial spherical particles instead of biological cells or with very limited variation in cell types. This paradigm should incorporate biological cells, which contain a much more advanced, intricate and meaningful biological structure to explore. In our latest work on NIC with human blood, (Zhang et al., 2024b), we have curated and classified human blood cells and other microscale targets, including RBCs, neutrophils, lymphocytes, platelets, HUVECs and PS particles. The proposed hybrid model CBAM-SNN accomplished a promising performance of 97% accuracy and F1 score with significantly reduced computation requirements. This work concluded that neuromorphic vision can visualise the convoluted structure, morphology and subtle differences between cells.

1.3 Discussion

Traditional FBSs are susceptible to degraded resolution when encountering high-speed objects, as these objects may pass through the field of view between frames or lack sufficient exposure time for proper sensor registration. A compromised throughput is inevitable for a desired resolution and has rendered the major roadblock for developing IFC. In addition, the generated image data can be cumbersome to process and commonly rely on manual operation by professionals for proper gating. This approach is also limited to the bivariate interpretation, which can fail to detect convoluted high-dimensional patterns.

This research introduced a novel method for handling high-speed objects with a minimum cost and resource. Before our first work Zhang et al. (2022), there was no preceding research on NIC. In this dissertation, each chapter covers a major milestone in NIC development, including the initial proof of concept, implementation of core cytometric functions, object detection with biological cells, and advanced ML analysis using a lightweight model on complex cell samples. Considering the continuous advancement of NIC, NVS and ML architecture, this paradigm can become a fundamental backbone for next-generation, Artificial Intelligence (AI)-enabled IFC.

1.4 List of publications

The publications listed below form the foundation of the main chapters of this thesis and are discussed in detail throughout the document.

1.4.1 Journal publications

- Zhang, Z., Xu, Z., McGuire, H. M., Essam, C., Nicholson, A., Hamilton, T. J., Li, J., Eshraghian, J. K., Yong, K.-T., Vigolo, D., et al. (2023). "Neuromorphic cytometry: Implementation on cell counting and size estimation." *Neuromorphic Computing and Engineering*, 3(4), 044005. `https://doi.org/10.1088/2634-4386/ad06c9`.
- Zhang, Z., Yang, H., Eshraghian, J. K., Li, J., Yong, K.-T., Vigolo, D., McGuire, H. M., & Kavehei, O. (2024). "Cell detection with convolutional spiking neural network for neuromorphic cytometry." *APL Machine Learning*, 2(2). `https://doi.org/10.1063/5.0199514`.

1.4.2 Conference publications

- Zhang, Z., Ma, M. S., Eshraghian, J. K., Vigolo, D., Yong, K.-T., & Kavehei, O. (2022). "Work in progress: Neuromorphic cytometry, high-throughput event-based flow imaging." In *8th IEEE International Conference on Event-Based Control, Communication, and Signal Processing (EBCCSP)* (pp. 1–5). `https://doi.org/10.1109/EBCCSP56922.2022.9845595`.

1.4.3 Other publications

- Huang, Z., Leung, W. H., Yu, L., Herbozo Contreras, L. F., Zhang, Z., Truong, N. D., Nikpour, A., & Kavehei, O. (2024). “On-device edge-learning for cardiac abnormality detection using a bio-inspired and spiking shallow network.” *APL Machine Learning*, 2(2). `https://doi.org/10.1063/5.0191571`.

1.4.4 Article under journal revision

- Zhang, Z., Yang, H., Li, J., Chong, S. W., Eshraghian, J. K., Yong, K.-T., Vigolo, D., McGuire, H. M., & Kavehei, O. (2024). Neuromorphic Imaging Cytometry on Human Blood Cells. `https://doi.org/10.1101/2024.11.16.623904`

- Herbozo Contreras, L. F., Yu, L., Huang, Z., Zhang, Z., Nikpour, A., & Kavehei, O. (2024). Tiny dLIF: A Dendritic Spiking Neural Network Enabling a Time-Domain Energy-Efficient Seizure Detection System. `https://doi.org/10.1101/2024.05.23.24307841`

Chapter 2

Our Early Demonstration of Neuromorphic Imaging Cytometry with Microscale Particle

This chapter proposes the first novelty and early demonstration of NIC. The preliminary discussion on adopting NVS over FBS for IFC and sorting application were highlighted. The experimental results of microparticle visualisation under NVS, visual quality via AT feedback, and application for optic flow were presented to support the hypothesis.

- Zhang, Z., Ma, M. S., Eshraghian, J. K., Vigolo, D., Yong, K.-T., & Kavehei, O. (2022). “Work in progress: Neuromorphic cytometry, high-throughput event-based flow imaging.” In *8th IEEE International Conference on Event-Based Control, Communication, and Signal Processing (EBCCSP)* (pp. 1–5). `https://doi.org/10.1109/EBCCSP56922.2022.9845595`.

Statement of Contributions of Joint Authorship

- Ziyao Zhang (Candidate): Experimental design, project conceptualisation, experimental work, literature review, data curation, hardware implementation, result evaluation, validation, article writing, reviewing and editing.
- Maria Sabrina Ma: Data analysis for optical flow and event display; article reviewing and editing.
- Jason K. Eshraghian: Expert advice on event data processing, neuromorphic operating principles, and neural network design; article reviewing and editing.
- Daniele Vigolo (Co-Supervisor): Expert advice for microfluidics, flow cytometry and cell sorting; microfluidic design and fabrication; article reviewing and editing.
- Ken-Tye Yong: Contributed to research methods, sample selection and microfluidic design; article reviewing and editing.
- Omid Kavehei (Principal Supervisor): Project conceptualisation, equipment acquisition, project administration, resources, supervision, result evaluation, validation, article writing, reviewing and editing.

In addition to the statements above, in cases where I am not the corresponding author of a published item, permission to include the published material has been granted by the corresponding author.

Ziyao Zhang Date: 22 February 2025

As supervisor for the candidature upon which this thesis is based, I can confirm that the authorship attribution statements above are correct.

Prof. Omid Kavehei Date: 22 February 2025

Cell screening and sorting technologies have been broadly adopted for medical diagnosis, cell-based therapy, and biological research. Microscopy operates with image capture that is subject to a highly constrained field-of-view, and even slow-moving targets may undergo motion blur, ghosting, and other movement-induced artefacts, which will ultimately degrade performance in developing machine learning models to perform cell sorting, detection, and tracking. FBSs are especially susceptible to these issues, and overcoming them with modern but conventional CMOS and CCD sensing technologies is highly costly. In this chapter, we provided our preliminary assessments and ideas on the merits of NVS over FBS for cytometry applications. We propose that implementing a neuromorphic sensory system or developing a new class of neuromorphic cameras customised for this purpose with our strategy will unbind the applications from the constraints of frame rate and provide a cost-efficient, reproducible, and high-throughput imaging mechanism. To demonstrate the feasibility of this early idea, we observed PS particles under neuromorphic vision at the beginning of this research, examining whether NVS can have the desired visual feedback in describing micro-scale objects with simplicity in shape. The experiment results on different durations of AT were presented, as AT plays a crucial parameter in collecting events to formulate visual representation and can also indicate the dynamics of the objects. The following chapters incorporate increasingly complex biological samples and analytical measures to consolidate the research approach and its functionality.

2.1 Introduction

Cell screening and sorting are indispensable in modern biological, medical, and biotechnological research fields (Nawaz et al., 2020; Shields Iv et al., 2015). Numerous devices are being developed to optimise emerging research needs. For example, IFC and Image-based Cell Sorting (ICS) are powerful strategies for studying cell morphology and behaviour, providing deeper insights into single-cell physiology (LaBelle et al., 2021). However, these applications face significant challenges inherent to frame-based sensory systems. Frame-based sensing in microscopy is limited to a narrow field of view. In flow imaging, this constraint causes even the slowest-moving cells to remain within the scene for a very short duration. This limitation worsens with increased magnification, leading to motion-induced artefacts like motion blur, which result in miscounting or misidentifying high-velocity targets and severely limiting processing bandwidth (Sesen and Whyte, 2020).

We are developing a neuromorphic-based image analysis system and screening instrument for cell screening and sorting platforms to address these challenges. An event camera, also known as NVS visualises dynamic events by detecting brightness changes in each pixel (Mueggler et al., 2017). Unlike frame-based systems with synchronous pixel readouts, NVS operate asynchronously, with pixels activated only in response to motion. This asynchronous operation eliminates motion blur and enables ultra-high-speed imaging. Our proposed NIC leverages the high bandwidth of low-cost event-based sensing to identify cell morphologies and classify them. The system integrates a microfluidic device to create dynamic contrast between target samples and the background, enabling high-throughput cell processing at increased magnifications without frame-rate constraints.

We have developed and open-sourced a neuromorphic training algorithm for cell identification. Specifically, we employ a spiking convolutional Long Short-Term Memory (LSTM) network capable of capturing 3D data streams. This network can classify cells in motion based on their external morphologies. During the initial development phase, the platform was tested with PS-based microparticles of varying sizes, confirming the sensor's ability to distinguish objects of different dimensions. Future efforts will focus on classifying live human blood cells and evaluating the system's performance in sorting them. Although our device is still developing, it has significant potential as a cost-efficient, reproducible, and high-throughput image-based cell screening and sorting system. The system aims to accurately distinguish cell morphologies and classify them into their respective categories, paving the way for advances in biological and medical research.

2.2 Related works

In recent years, ICS has shown great potential in regenerative medicine and cancer immunotherapies (LaBelle et al., 2021). An ICS platform conventionally pairs image acquisition with a computational analysis tool for cell sorting. The high density of cell count leads to throughput challenges in both sensing and processing (Isozaki et al., 2020b).

The study conducted by Isozaki et al. (2020b) demonstrates using a sequentially addressable dielectrophoretic array to attain high-throughput cell sorting for large-volume droplets. They successfully achieved up to 20 times higher sorting efficiency than conventional approaches. The cells can also be sorted within a large droplet (100 pl). Their proposed method provides a more stable, viable, and nutritional environment for the sample cells. This technology deployed a high-speed camera (Phantom v2640, Vision Research, USA) to track the sorting trajectory and provide visual feedback on the platform. Although the device yielded the desired outcome, using high-power, professional-grade, state-of-the-art camera sensing can be an overbearing cost for research and start-up projects.

Other applications, such as the dual-imaging cell sorting system developed by Sesen and Whyte (2020), have created a label-free, ease-of-use platform that yields high-purity output. Their findings highlighted the inherent limitation of throughput, which can be partially resolved by replacing the input camera with a more advanced detecting strategy. Deploying a neuromorphic sensory system can substantially mitigate the issue of motion blur and miscounting of cells.

Despite the increasing traction in developing image-enabled cell screening and sorting platforms, high-speed neuromorphic sensing, though naturally suited for cytometry, has not yet been harnessed. The following sections describe our work-in-progress high-throughput neuromorphic system for cell counting and sorting.

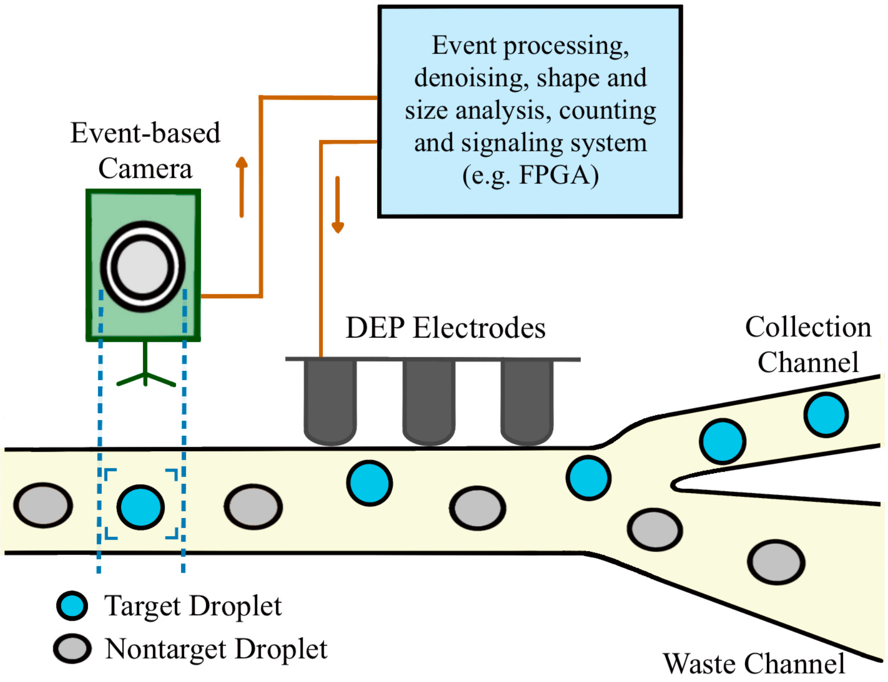

Figure 2.1 – Illustrative schematic of our neuromorphic flow imaging cytometry, inspired by (Sesen and Whyte, 2020). The droplet image was captured using the event-based camera and passed into a preliminary model for decision-making and output activation of the DEP electrodes. FPGA is a field programmable gate array for ultra-high-speed and reconfigurable real-time data analysis.

2.3 Methodology

2.3.1 Sample preparation

The initial testing of our neuromorphic-based detection system was conducted using PS microparticles to demonstrate the working principle. 10 wt% concentrated 3 μm, 8 μm, and 15 μm microparticle solutions were purchased (Sigma-Aldrich, USA) to resemble the size of human blood cells (e.g., platelet, erythrocyte, leukocyte) and abnormal cells (e.g., cancer cells). The particle solutions were diluted 1:100 with deionised water and vortexed. This procedure ensures the particles' concentration or spacing is evenly dispersed, avoiding possible aggregation. The particles were then delivered to a microfluidic chip to extract and classify their external features via a neuromorphic camera.

2.3.2 Towards microfluidic imaging sorting platform

A 100 μm thick, 1 mm wide and 40 mm long microfluidic chip was fabricated using a standard photolithography protocol. The chip contains one inlet channel and one output channel for essential observation study, evaluating the feasibility and imaging performance of the neuromorphic device in capturing microscale targets. The microparticle solution was allocated into the inlet and actuated forward to the delivery channel by applying additional pressure via a syringe pump. In the early stage of development, we adopted a neuromorphic camera, Evaluation Kit 3 (EVK3) (Prophesee, France), which was attached to the microscope to monitor the dynamics of the section of interest in the delivery channel. As the particles passed through the narrow field of view, the size and morphology of the sample particles were collected and uploaded for post-processing.

In future development, the proposed platform will include a microfluidic chip with three inlet channels and two output channels for conducting droplet generation and sample collection functionalities. DEP electrodes will be placed on the upper side of the main delivery channel to induce force on target droplets, which can displace the direction of travel based on the sorting decision. Once the decision has been made, the target droplets receive a positive force from the electrodes, which gradually pulls the droplets into the track of the collectable output channel. Non-targeted droplets do not receive intervention and enter the waste output outlet by default geometrical design.

2.3.3 Microparticle experiment

The experiment investigated microparticles in 3 μm, 8 μm, and 15 μm. This procedure aims to verify the capacity of asynchronously activated pixels in tracking microscale objects, estimating the possible performance for actual cells. 1 mL of the diluted microparticle solution was loaded into a 1 mL syringe and placed on a syringe pump. The flow rate was set at 10 μL/min for uniformly distributing the particles. Once the delivery was initiated, the neuromorphic camera recorded all dynamics in the field of interest. In addition, the baseline was constructed by extracting the raw imaging from standard-used inverted microscopy for comparison study.

2.3.4 Model development

Using an object classification algorithm, the proof-of-concept model aims to distinguish particles of different sizes. A typical neural network is conventionally trained to extract morphological features of the cells (e.g., shape and colour) (Sciambi and Abate, 2015). High-speed event cameras can capture second-order effects that arise from these morphological markers of cells, such as the dynamics of the air trails within the fluid walls. While microfluidic analysis typically requires the elimination of air-induced artefacts, such as by detaching air bubbles from the path, it is expected that our use case can benefit from these additional features by accounting for data that is not retained in static images, including speed, cytoplasmic viscosity, and density. A sample of fluidic trails captured by our system is illustrated in Fig. 2.3.

A sequential neural network is required to extract features from long-range temporal dependencies across the brief instance the cell crosses the frame in Fig. 2.1 and the subsequent lengthy period the fluid trails are visible. At present, we are testing two types of sequential neural networks. One is a conventional SNN consisting of leaky integrate-and-fire neurons modelled by the following dynamics:

$$\tau \frac{dU}{dt} = -U + I_{\text{in}}R,$$

where U is the membrane potential of a spiking neuron, I_{in} is the input current injection triggered by input events in the first layer, and R is the effective resistance of the thin film membrane (Buggenthin et al., 2017). An approximate solution can be derived using the forward Euler method:

$$U_{t+1} = \beta U_t + (1 - \beta) I_{\text{in},t},$$

where $\beta = e^{-1/RC}$ is the inverse time constant of U. The full derivation can be found in Lapicque (1907). When U_t exceeds a threshold θ, a spike is emitted to downstream connections. Surrogate gradient descent is used to overcome the non-differentiability of spikes during error backpropagation (Eshraghian et al., 2023a; Neftci et al., 2019a).

SNNs are modelled as recurrent networks, so their capacity to learn temporal dependencies is limited (e.g., on the order of 10s of sequential steps). The second type of SNN that we use to address this issue is a spiking convolutional LSTM network (Eshraghian and Lu, 2022; Schmidhuber et al., 1997). The convolutional operator accounts for spatial feature extraction, the LSTM cell learns temporal relations in the data, and a hard threshold is applied to the hidden state, treated as the membrane potential U, to elicit spike-based dynamics. The spike-based operation reduces computational overhead by constraining layer-to-layer communication to a single bit. We apply a straight-through estimator to account for spiking non-differentiability in this network.

While several spiking variants of long short-term memory have been proposed, our approach to spiking LSTMs has been open-sourced and integrated with the deep learning framework, snnTorch, available at the following URL: `https://github.com/jeshraghian/snntorch`.

2.4 Preliminary results and discussion

While this work remains in progress, a concept simulation utilising heterogeneous microparticles has been concluded, estimating the possible imaging performance when observing actual cells, thus suggesting that cell morphologies can perceptibly be distinguished when streamed as events. In the interim, we present some estimated merits of our platform and fundamental results.

The primary benefit of using an event-based input system is the high-speed, low-cost mode of data capture achieved by decoupling from the need for frame-based streaming. As flow velocity can be 3 m/s for fast cell sorting (30 kHz) (Sciambi and Abate, 2015), the target sample can pass through the region of interest without being

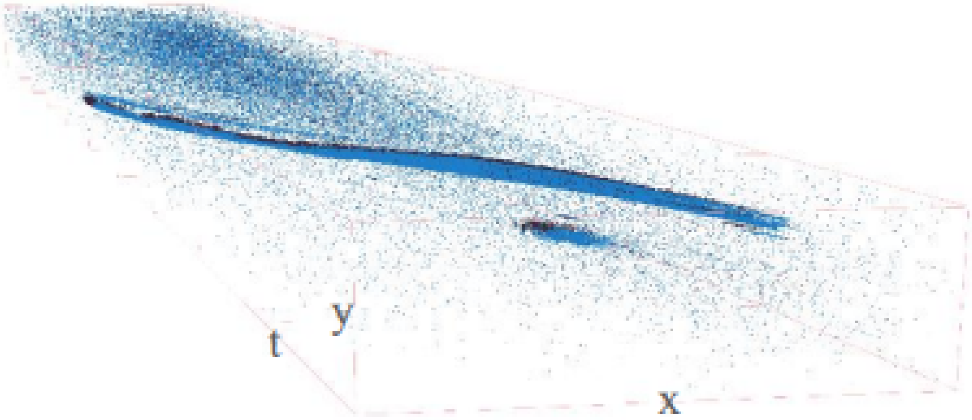

Figure 2.2 – Real-time display of the events in the form of (x, y, p, t), where x and y are the horizontal and vertical positions of the event on the frame, t is the time, and p is the polarity (blue represents moving forward while black represents moving backwards). The trails of the objects can be seen clearly on the graph, which is moving concerning time. Noise removal has not been applied to show the raw data capture.

recorded by the next frame. This can lead to major miscounting, ghost detection, and is a general technical limitation to throughput (Sesen and Whyte, 2020). As shown in Fig. 1.1, overcoming this issue using conventional frame-based systems can cost around $100,000 AUD for professionally graded high-speed camera systems.

Thus, our platform aims to provide a more cost-friendly and practical approach that lowers the barrier to experimenting with neuromorphic cytometry and microscopy for academic and resource-limited laboratories. However, as our device is still in the preliminary phase, a few aspects need to be considered, including the difficulties of identifying similar cell morphologies, the non-contact limit of accessing cell contents, and developing a sorting algorithm that can match the throughput of the high-speed sensing system. In future development, human cells and other cell lines will be investigated to quantify how much these limitations affect the platform's overall performance.

As shown in Fig. 2.2, the motion of the particles can be seen over time, demonstrating the platform's feasibility in tracking the object's trajectory. Upon completion of the dataset curation phase, the events captured by the camera will be processed by our

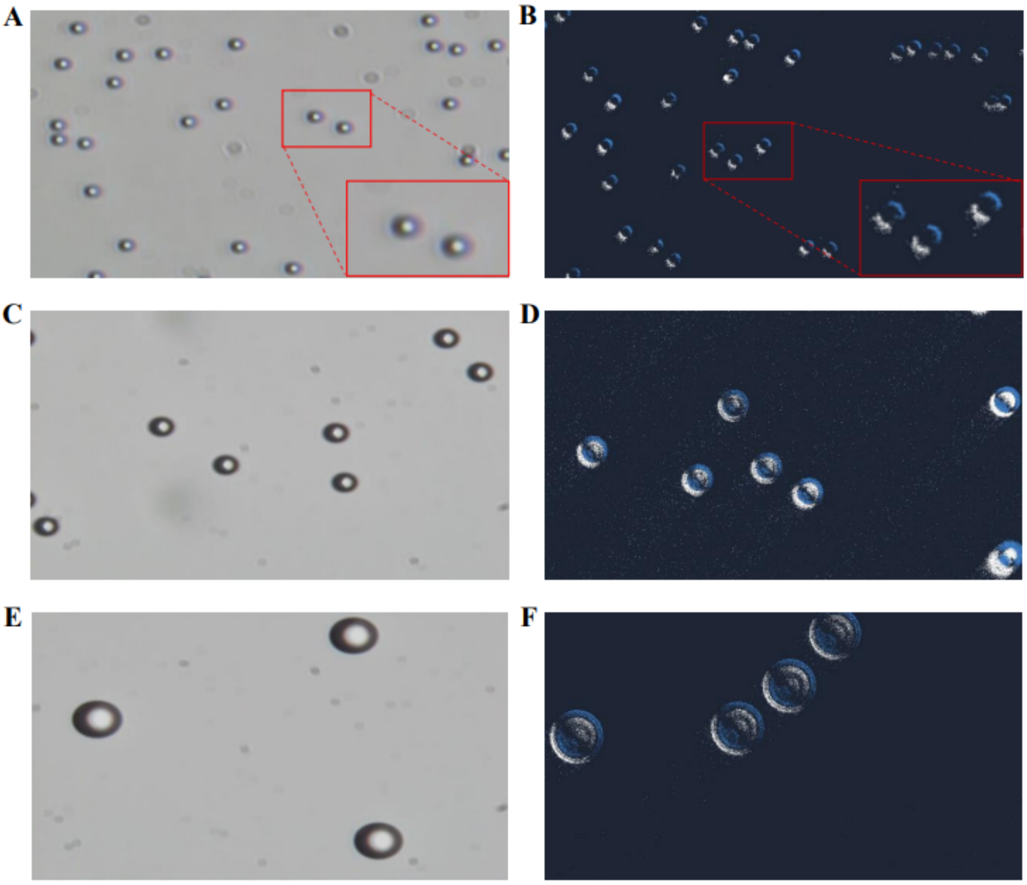

Figure 2.3 – Real-time imaging of the microparticles in the sizes of 3 μm, 8 μm, and 15 μm were taken by a conventional inverted microscope and a neuromorphic camera. The comparative imaging were taken at different time intervals. (A) 3 μm microparticle image captured by a conventional microscope. The red-marked section presented a 1.5× magnified visualisation of the microparticles. (B) 3 μm microparticle captured by a neuromorphic camera. (C) 8 μm microparticle captured by a conventional microscope. (D) 8 μm microparticle captured by a neuromorphic camera. (E) 15 μm microparticle image captured by a conventional microscope. (F) 15 μm microparticle captured by a neuromorphic camera.

SNN classification algorithm, which can distinguish various cell morphologies and realise effective cell sorting.

In a later stage, a microscope with a higher magnification objective will be integrated into the system so that the camera can be used to directly capture the cell morphologies and motions, which will form the basis of this proposed work. With the completion of the preliminary experiments, the proposed project will continue

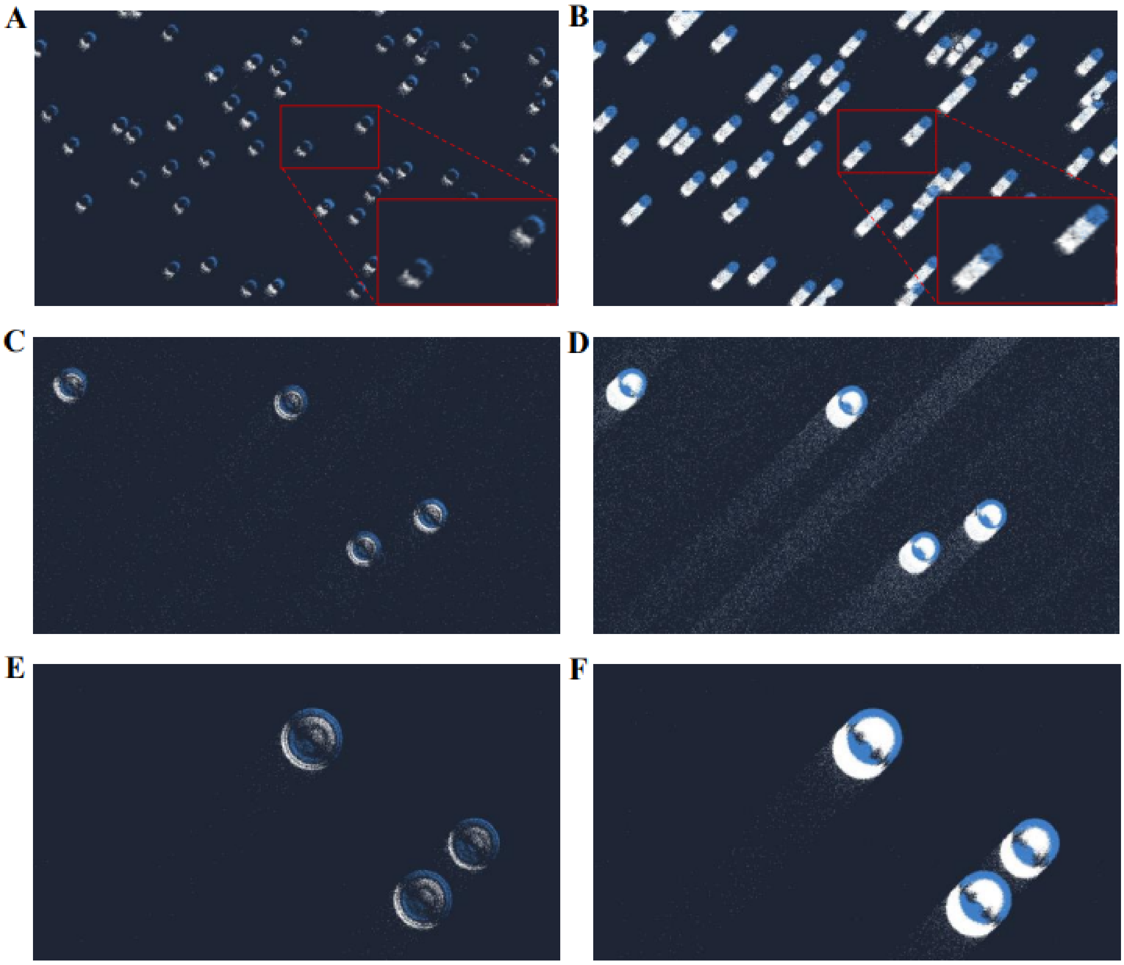

Figure 2.4 – Neuromorphic imaging of the targeted microparticles were recorded at 1 ms and 10 ms AT. (A) 3 μm microparticles motion recorded at 1 ms AT. The red-marked section presented a 1.5× magnified visualisation of the microparticles. (B) 3 μm microparticles motion recorded at 10 ms AT. (C) 8 μm microparticles motion recorded at 1 ms. (D) 8 μm microparticles motion recorded at 10 ms. (E) 15 μm microparticles motion recorded at 1 ms. (F) 15 μm microparticles motion recorded at 10 ms.

dataset curation and move on to the primary experimental stage, which focuses on implementing the sorting system and algorithm development, training, and testing.

The device's imaging performance was evaluated and contrasted with conventional inverted microscopic imaging in Fig. 2.3. The contour of the microparticles in each size can be clearly defined via an event-based camera, providing a solid training resource for sample classification and decision-making. Another significant intrinsic advantage of the neuromorphic camera is that any static component of the image, such as the microparticles adherent to the channel's internal structure, was automatically neglected during the recording due to the peculiar way event cameras work. Background subtraction is often required to improve the detection and cell recognition capabilities. In our proposed approach, only a change in contrast is detected due to the motion of particles. Thus, static spurious contributions are automatically neglected, representing an advantage for future neuromorphic cytometry implementation. With further development in denoising, this technology has the potential to reconstruct data that is information-rich without typical vision-sensing limitations.

The neuromorphic imaging of the targeted microparticles was recorded at 1 ms and 10 ms AT in Fig. 2.4. The distinct morphology and sizes were revealed during the delivery, proving that our technology can identify moving objects at the equivalent frame rate of $1,000$ fps and 100 fps. Moreover, the proposed event-driven visual system has not been optimised yet for speed. Additional development on the subject will contribute to an equivalent frame rate of over $10,000$ fps. The confirmed outcomes and imaging of the microparticles attested to the feasibility of our device and the conceptual potentiality of developing an industrial or laboratory-used cell sorting strategy.

The optical flow method can visualise the apparent motion involved in moving objects, and it has broad utilisation in object tracking, movement detection, and robotic navigation (Benosman et al., 2012). It is also capable of evaluating the post-administration performance of a variety of medical imaging and treatment devices for intracranial aneurysms, thrombus, and other complexities (Morais et al., 2022; Pereira et al., 2013). As shown in Fig. 2.5, the visual pattern of the dynamic motion of the microparticles is vectored, indicating that our event-driven visualisation system can be adopted for a real-time optical flow analysis of microscale targets and its relevant clinical usage.

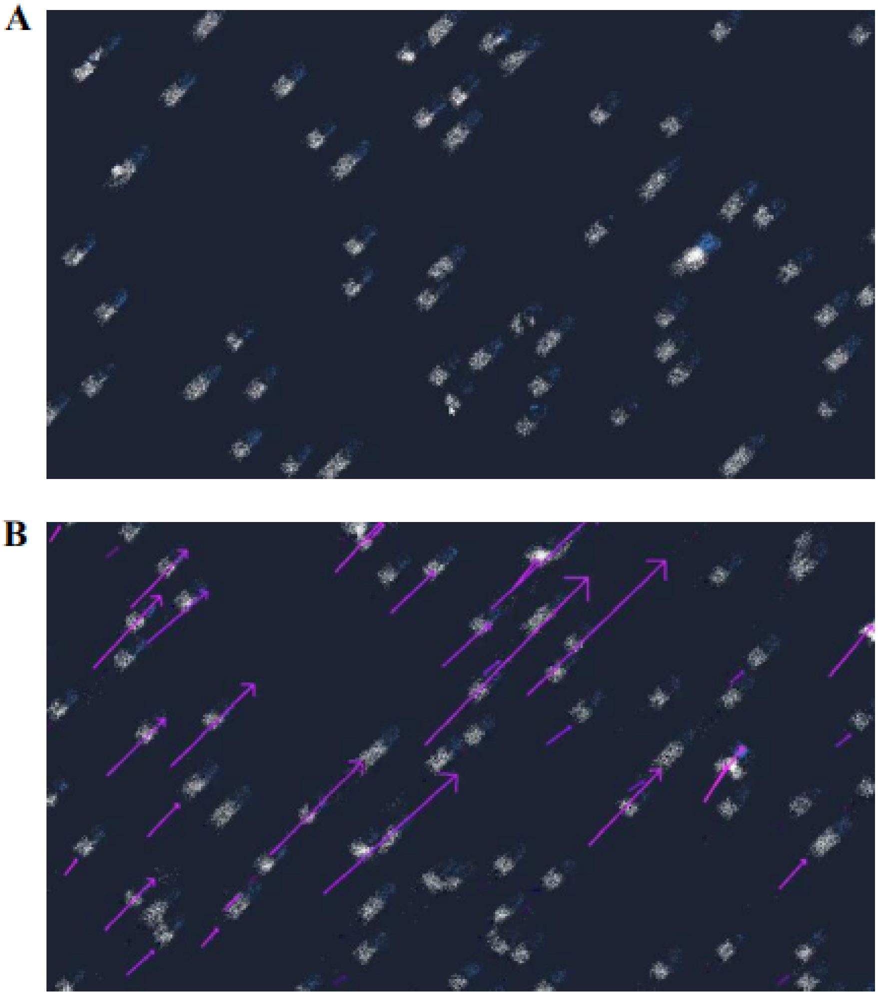

Figure 2.5 – Optical flow estimation of the flowing microparticles, denoised by the Spatiotemporal Contrast Filter. The comparative imaging was taken at different time intervals. (A) 3 μm microparticles at the flow rate of 10 μL/min. (B) 3 μm microparticles at the flow rate of 10 μL/min with motion marked using the optical flow method.

2.4.1 Conclusion

While other cytometry functions and analyses are put forward in this ongoing instrumentation work, we understand that high cell content screening requires speed to capture and deal with significant numbers of cell morphology analyses to be statistically relevant (Buchser et al., 2014; Cossarizza et al., 2019; Rane et al., 2017; Stirling et al., 2021). Low-cost cameras often cannot provide high frame rate imaging, but larger image sensors address this to provide larger fields. Neuromorphic kinetic imaging can combine ultra-fast videography with high-throughput analytics to, in real-time, understand and measure the early morphological and kinetic effects of therapeutic candidates in a significant content of cells (Buchser et al., 2014).

Chapter 3

Implementation of Cell Counting and Size Estimation with Demonstration of Superior Fluorescence Sensitivity

In this chapter, we implemented the functions of cell counting and size estimation similar to what a conventional FC can provide. The platform demonstrated a competitive performance compared to a commercialised FC. This chapter also curated the crucial proofs for the advanced fluorescence sensitivity of the proposed architecture. The content presented in this chapter is published as:

- Zhang, Z., Xu, Z., McGuire, H. M., Essam, C., Nicholson, A., Hamilton, T. J., Li, J., Eshraghian, J. K., Yong, K.-T., Vigolo, D., et al. (2023). "Neuromorphic cytometry: Implementation on cell counting and size estimation." *Neuromorphic Computing and Engineering*, 3(4), 044005. `https://doi.org/10.1088/2634-4386/ad06c9`.

Statement of Contributions of Joint Authorship

- Ziyao Zhang (Candidate): Experimental design, project conceptualisation, experimental work, literature review, data curation, result evaluation, validation, data analysis, software programming, function implementation, article writing, reviewing and editing.

- Helen M. McGuire (Co-Supervisor): Expert advice on cell biology, immunology and flow cytometry; sample preparation, experimental work, data analysis, article reviewing and editing.

- Chip Essam: Contributed to sensor development, device integration, data curation, data analysis, article reviewing and editing.

- Andrew Nicholson: Contributed to sensor development, device integration, data curation, data analysis, article reviewing and editing.

- Tara J. Hamilton: Contributed to sensor development, device integration, data curation, data analysis, article reviewing and editing.

- Jiayin Li: Experimental work, data visualisation, data analysis, article reviewing and editing.

- Jason K. Eshraghian: Expert advice on event data processing, neuromorphic operating principles, and neural network design; article reviewing and editing.

- Daniele Vigolo (Co-Supervisor): Expert advice for microfluidics, flow cytometry and cell sorting; microfluidic design and fabrication; article reviewing and editing.

- Ken-Tye Yong: Contributed to research methods, sample selection and microfluidic design; article reviewing and editing.

- Omid Kavehei (Principal Supervisor): Project conceptualisation, equipment acquisition, project administration, resources, supervision, result evaluation, validation, article writing, reviewing and editing.

In addition to the statements above, in cases where I am not the corresponding author of a published item, permission to include the published material has been granted by the corresponding author.

Ziyao Zhang Date: 22 February 2025

As supervisor for the candidature upon which this thesis is based, I can confirm that the authorship attribution statements above are correct.

Prof. Omid Kavehei Date: 22 February 2025

IFC is a powerful analytic tool that combines the principles of conventional FC with rich spatial information, allowing more profound insights into single-cell analysis. However, offering such high-resolution, full-frame feedback can restrain processing speed and has become a significant trade-off during development. Notably, the DR of traditional FBS can fail to capture subtle fluorescence emissions or fluorescent targets travelling at high velocity. Fluorescence probes are essential for characterising proteins, enzymes, and biomolecules in a living cell; however, their detection can be challenging as many of these molecules exist in trace amounts. Neuromorphic photosensing focuses on the events of interest via individual-firing pixels to reduce data redundancy and latency. With its inherent HDR (>120 dB), this architecture has the potential to drastically elevate the performance in throughput and sensitivity to fluorescent targets. In this chapter, we presented an early demonstration of NIC, evaluating the feasibility of implementing cytometric-like functions for object counting and size estimation to measure 8 μm, 15 μm microparticles and THP-1 cells. Our work has achieved highly consistent outputs with a widely adopted FC, CytoFLEX, in detecting microparticles. Moreover, the capacity of a NVS in registering fluorescent signals was evaluated by recording 6 μm FITC-marked particles in different excitation conditions, revealing superior performance compared to a standard CMOS.

3.1 Introduction

Conventional FC is a vastly adopted high-throughput technology that is capable of measuring multiparametric features of cells in a population, including cell count, relative size, granularity, and can be combined with fluorescence detection for additional phenotypical characterisations (Drescher et al., 2021; Li et al., 2021). It can analyse over 10,000 events per second to generate instant feedback on samples (Rees et al., 2022). However, such a high-speed approach is limited to lower-dimensional feedback and lacks subcellular resolution (Schraivogel et al., 2022). Thus, numerous applications have been developed to optimise various emerging research needs.

IFC is one of the remarkable strategies that combines features of high efficiency in FC with detailed spatial information and fluorescence intensity (Barteneva et al., 2012; Rees et al., 2022). It can comprehensively visualise cell area with more intricate metrics, including cell morphology, texture, correlation and marker localisation in high-resolution feedback (McKinnon, 2018). As with every invention, the FBS adopted in IFC can suffer from inherent constraints that hinder its performance in delivering high throughput results while maintaining rich spatial information. Considering the limited field of view provided by microscopy or the interrogation point in IFC, cells in the flow can only remain within the bounds of the scene for an extremely brief period. Frame-based capturing techniques can be vulnerable to consecutive fast-moving targets, especially in equipment with high frame intervals. High-speed objects between two frames can lead to motion blur, ghost detection and other motion-induced artifacts (Sesen and Whyte, 2020).

Immunofluorescence is an essential analytic technique that utilises fluorophore-coupled antibodies to identify the localisation of various cellular components within cells, tissues and 3D culture-derived cellular spherical structures (Joshi and Yu, 2017). Combining with IFC, this strategy is particularly useful for revealing cell signalling, co-localisation, cell-to-cell interaction and DNA integrity in large-scale populations (McKinnon, 2018). Many target components such as proteins, enzymes and biomolecules exist in trace amounts or fluctuate, rendering poor visualisation or absence of information during detection(Hirano et al., 2022; Izumi et al., 2009; Li et al., 2023; Nagai et al., 2004; Vinegoni et al., 2018, 2016). The DR of current photosensors can have difficulties perceiving limited fluorescence signals, and overexcitation from light sources can lead to phototoxicity, photobleaching and tissue heating on cells (Li et al., 2023). These further exacerbate the trade-off relationship between speed, sensitivity and spatial resolution (Huang et al., 2022). Increasing the throughput of IFC without jeopardising other parameters remains one of the outstanding obstacles in the field of IFC (LaBelle et al., 2021). These inspired us to develop a data- and cost-efficient fluorescence-sensitive high-throughput cytometry to challenge these conundrums.

Neuromorphic vision can detect objects in motion by individually adapting brightness changes in each pixel, and when there is no motion included in the field, pixels will remain inactivated (Mueggler et al., 2017). This is compared to a frame-based pixel array synchronously timed to a global shutter. The unique mechanism in neuromorphic allows real-time processing with low latency, leading to great application in object tracking, recognition and motion analysis (Yang et al., 2022). As the maximum detection range of fluorescence signal is highly dependent on the DR of the applied sensor (Vinegoni et al., 2018), the HDR (>120 dB) provided by an event-based photodetector can be an ideal candidate for visualising fluorescence-tagged objects, especially in low lighting or dark scenarios. To evaluate the possibility of integrating neuromorphic vision as a substitution for frame-based sensors in IFC and its feasibility of visualising microscale targets, the experiments were carried out with different sizes of PS microparticles and THP-1 cells flowed within a microfluidic channel to create the essential dynamic contrast between targeted objects and the background for neuromorphic imaging. Herein, we are delivering an early demonstration of neuromorphic cytometry to perform object counting and size estimation on microscale particles and THP-1 cells, presenting the first instance of neuromorphic-enabled cell measurements and building upon our previous endeavour on introducing neuromorphic architecture as an alternative to overcome the conventional frame-related challenges in IFC.

3.2 Relevant Works

IFC can offer rich spatial information regarding cell interpretation; however, as with many imaging systems, It is also bound to the triangle of imaging constraints – speed, sensitivity and resolution. Increasing one of the parameters can lead to degradation in others (Rees et al., 2022). In contrast, event-based cameras are more robust in handling low-lighting conditions and highly dynamic scenes owning to their asynchronous firing pixels, and the high-resolution event data can support over ≥ 3 μs frame-rate (Pan et al., 2020). The study conducted by Howell et al. (2020) evaluated the performance of a dynamic vision sensor in detecting fluorescent objects flowing in a spiral microfluidic device and proved the visualisation. Adopting an event-focused vision and architecture can significantly reduce the data redundancy and possibly elevate the performance in throughput and sensitivity without or with a minor reduction in resolution. He et al. (2022) utilised the neuromorphic-enabled imaging classification, accomplished a mean average precision of 98.52% at a speed of over 1000 fps and performed 3D reconstruction of the measured subjects via intensity and contour extraction. Moreover, the recent work conducted by Abreu et al. (2023) utilising an event-based camera to conduct binary particle classification with a SNN and achieved 98.45% testing accuracy, which further consolidates the feasibility of implementing neuromorphic architecture in the field of cytometry. To the best of our knowledge, our previous work, Zhang et al. (2022), is one of the first feasibility demonstrations of conceptualising and building a neuromorphic-enabled IFC, delivering early imaging of microscale objects under an event-based vision. All these endeavours indicated the potential of adopting a neuromorphic vision and architecture in providing cell measurements, exhibiting a high level of accuracy and possible advanced throughput of neuromorphic cytometry.

3.3 Method

3.3.1 Sample preparation

PS-based microparticles were prepared in the initial testing to evaluate the performance of neuromorphic vision in capturing microscale targets. 10 wt.% concentrated 8 μm and 15 μm microparticle solutions were acquired (Sigma-Aldrich, USA) to emulate the relative size of human blood cells (erythrocyte, leukocyte) and abnormal cells (e.g., cancer cells). 8 μm particle solution was diluted in 1:250 with deionised water to maintain a sufficient count and spacing between particles, preventing statistical inadequacy in sample size and possible aggregation. As the concentration of the particles was distributed by weight, 15µm particle solution was diluted in 1:38 to obtain a similar number with diluted 8 μm particles. Once the dilutions were completed, the sample particles were introduced into respective microfluidic channels to acquire neuromorphic feedback on counting and size estimation. To establish a baseline comparison, the same concentrations of the particles were prepared and analysed by a FC (CytoFLEX, Beckman Coulter) to obtain the measurement of counts and sizes to ensure the validity of the results.

Human monocytic cell line, THP-1 cells were collected from Barry Slobedman laboratory in the Charles Perkins Centre at The University of Sydney. The cells were maintained in a 37 °C and 5% CO_2 incubator and harvested in this experiment to examine the compatibility of neuromorphic vision with real sample cells and determine whether the complexity in cells can degrade or impact the visualisation and detection algorithm. The targeted cell line was prepared at the concentration of 1×10^6 cells/mL. The cell solution was first centrifuged at a speed of 400 g for 5 minutes for sample separation. Then, the cell pellet was collected cells and re-suspended with a FC buffer made of 0.02% sodium azide, 0.5% Bovine Serum Albumin (BSA) and 2 mM Ethylenediaminetetraacetic Acid (EDTA) in Phosphate-Buffered Saline (PBS). The sample solution was vortexed and equally distributed into aliquots for neuromorphic analysis and CytoFLEX baseline comparison.

3.3.2 Microfluidic imaging platform

A 60 μm-height and 100 μm-width microfluidic chip was fabricated utilising a standard photolithography protocol (Zaouk et al., 2006). The chip contains one inlet and outlet channel to create an essential delivery and visualisation pathway for the target samples. In addition, the channel employed a height of 60 μm to focus the particles into a relatively limited plane to avoid a broad depth range and excessive calibration caused by it. In this platform, an event-based camera, EVK4 (Prophesee, France), was integrated into a microscope (IX73 Inverted Microscope, Olympus, Japan) for proper magnification (10×) of the microscale objects and monitoring the dynamics of the field of view at the centre of delivering channel.

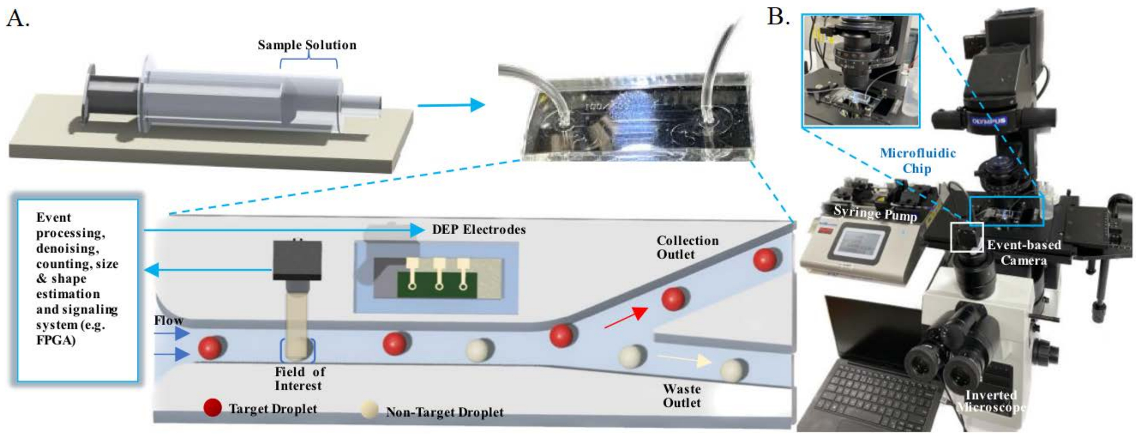

Figure 3.1 – A) Proposed schema of neuromorphic cytometry. The target samples were introduced into the microfluidic channel in a flow. Features of the samples were captured by a NVS, sending the inputs into the processing unit for classification and sorting purposes. After decision-making, the target object was directed into the collection channel via a DEP sorter. (B) The current setup of the platform with an event-based camera integrated into a microscope for recording and capturing the sample flow.

3.3.3 Microparticle and cell experiments

The microparticles in the size of 8 μm and 15 μm and THP-1 cells were adopted in this experiment to investigate the capacity of asynchronously activated pixels in tracking microscale objects. The diluted sample solution was loaded into a 1 mL syringe and distributed into the channel by actuation of a syringe pump (LEGATO 200 Syringe Pumps, KD Scientific Inc, USA) at the flow rate of 10 μL/min. As the objects travelled through the section of interest, the physical characteristics of the targets were collected and later analysed for object counting and size estimation using the modified `metavision_psm.py` provided by Prophesee. The same dilution factor was applied to the samples and analysed via CytoFLEX to provide outputs on total counts and estimated sizes for the baseline comparison.

3.4 Results

The proposed schematic of our NIC is illustrated in Fig. 3.1 to demonstrate the working principle and expected future implementation. As the sample flow is introduced

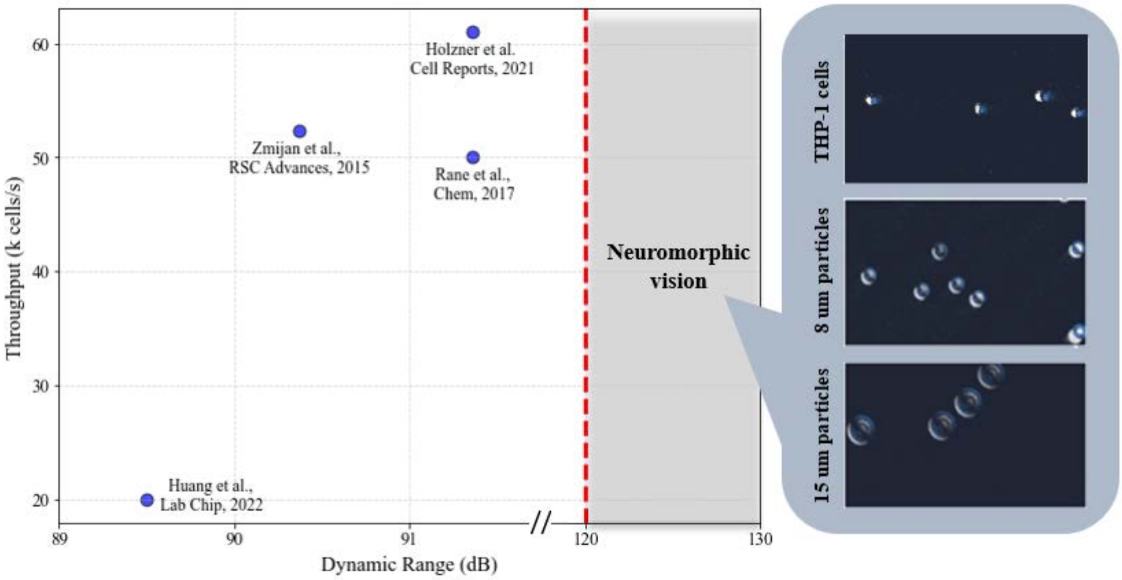

Figure 3.2 – Performance of the previously reported fluorescence IFC with their incorporated DR. The grey shade highlighted the unattained outputs and DR provided by the neuromorphic vision and sample imaging of different microscale targets. Cited papers in this figure are Huang et al. (2022), Zmijan et al. (2015), Holzner et al. (2021), Rane et al. (2017).

into the channel, the neuromorphic sensor will detect the ongoing subjects once it enters the view. The captured imaging will be fed to the processing centre for denoising, filtering, object counting, size and morphology estimation, determining whether the object is of interest and sending a signal to the DEP sorter for sorting decisions. Once the DEP device receives the outcome, the electrodes gently pull the targeted object into the pathway to the collection outlet. The unaltered objects will enter the waste outlet by default geometrical design.

One of the novel attempts that should be continuously explored with neuromorphic sensors is the ability of HDR to capture high-speed fluorescent objects. Fig. 3.2 illustrates the documented throughput of fluorescence IFC with their respective DR, and the work published by Vinegoni et al. (2018) highlighted that the maximum capacity of the fluorescence detected is majorly dependent on the DR provided. Even though recent efforts have achieved a high throughput with high-resolution imaging in detecting fluorescence-tagged objects, these works, while remarkable, only adopted compensation strategies such as time-delay integration and virtual-freezing technique,

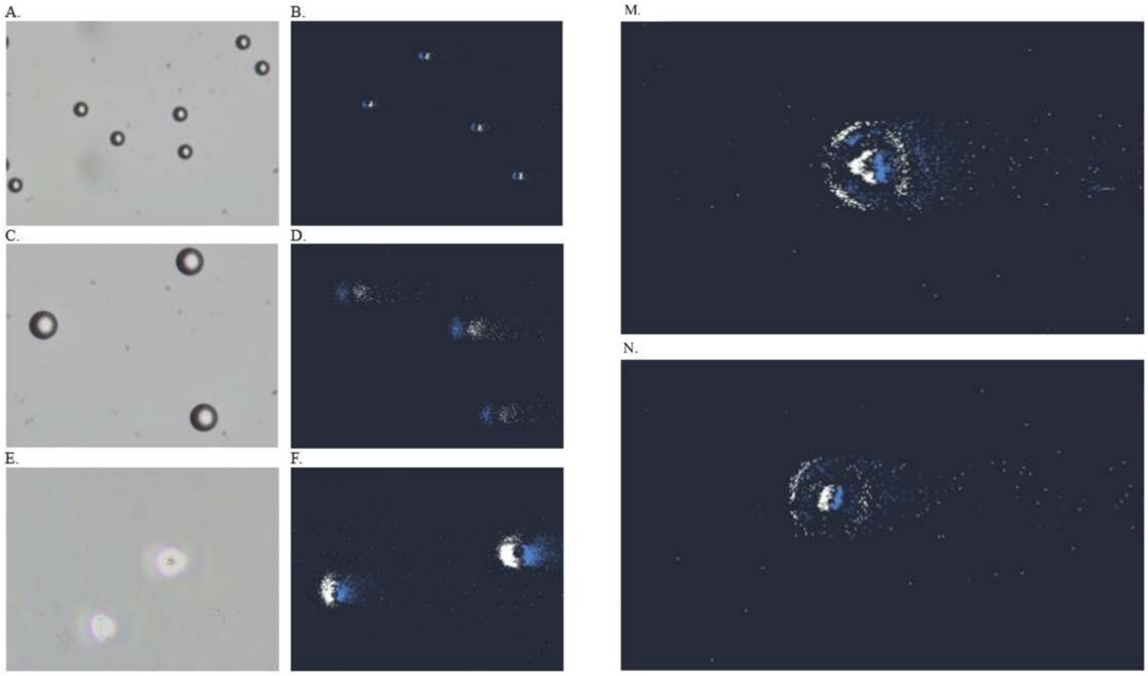

Figure 3.3 – Conventional microscopic imaging and neuromorphic imaging of 8 μm, 15 μm microparticles and THP-1 cells. (A),(B) Microscopic and neuromorphic images of 8 μm microparticles. The neuromorphic image on 8 μm microparticles. (C),(D) Microscopic and neuromorphic images of 15 μm microparticles. (E),(F) Microscopic and neuromorphic images of THP-1 cells. (M),(N) Nucleus-like objects in MCF-7 cells captured by neuromorphic vision under 20× magnification.

the direct correlation and performance of HDR in registering fluorescence signals remain unknown. To our knowledge, there has not been an IFC that exploited such a HDR (> 120 dB) compared to the neuromorphic camera, future endeavours on the subject can be highly informative and promising in developing next-generation IFC.

At the current stage, our platform can visualise and perform measurements on the basic physical properties of microscale objects. In Fig. 3.3 (A)-(F), the precise contour and relative size difference in neuromorphic view can be observed and compared to a phase contrast vision under a conventional microscope (ECLIPSE Ts2-FL, Nikon, Japan). Both imaging techniques were competent in delivering essential visual feedback without losing the key integrity of the subjects. In addition, when conducting microfluidic delivery with microscale targets, some of the travelling objects will inevitably adhere to the internal surface of the channel, rendering multiple imaging obstructions and deviating the focus from subjects. In neuromorphic, as the necessary

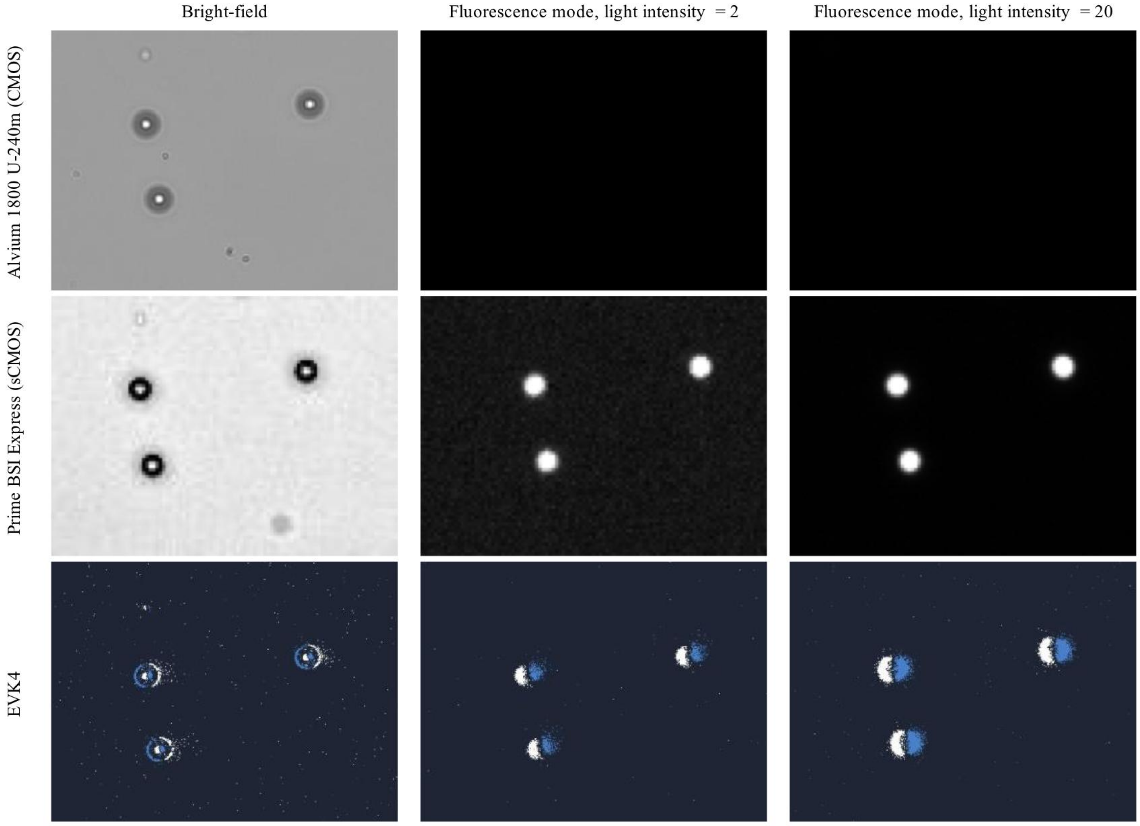

Figure 3.4 – Microscopic imaging captured by Alvinum 1800 U-240 m (CMOS), Prime BSI Express (sCMOS) and EVK4 under varying illumination conditions. The first column on the left illustrated the images captured under a bright-field. The second column indicated the images taken in a fluorescence mode with light intensity set on 2 in the blue light region. The third column illustrated the images taken with light intensity set on 20 in the blue light region.

movements are required to create the contrast between objects and the background, objects that remain in a static position will not activate the pixels. This unique architecture can mitigate that consequential image effect caused by attached objects, significantly reducing the labour required for post-imaging processing and focusing on subjects of interest.

The sensitivity of EVS to fluorescent signals was compared to a standard CMOS, Alvium 1800 U-240 and sCMOS camera, Prime BSI Express. In Fig 3.4, the visions of three cameras were revealed. All cameras can deliver visual feedback on FITC particles with essential features intact in a bright field. As the illumination was turned into fluorescence mode, the traditional camera lost its ability to detect any object in a dark background regardless of the intensity of the excitation light. On the contrary, the sCMOS sensor and Event Vision Sensor (EVS) can depict the spatial content with lower and higher excitation (2 and 20). The difference in the sCMOS camera under weak and higher excitation power is that when the object is excited by the weak illumination, the image shows more background noise during detection, and higher illumination can lead to a more well-defined sample imaging with minimised background noise. With EVS, both lighting conditions can lead to visualisation without a noticeable increase in noise. Owing to the high quantum efficiency (∼95%), dynamic range (74.98 dB), and aid of auto-contrast provided by Micro-Manager software, the sCMOS sensor has focused and distinct visual feedback in presenting fluorescent targets. However, offering such high sensitivity leads to a compromised frame rate, which only tolerates 43 fps at full resolution (2048×2048, 16-bit) and a maximum of 1,468 fps with reduced frame resolution (2048×128, 11-bit). On the other hand, EVS can support over 10,000 fps while maintaining its current sensitivity to fluorescent targets without any strategy of imaging processing. We believe that in the context of static imaging, a sCMOS such as Prime BSI Express can generate outstanding resolution and sensitivity; However, in a highly dynamic scene, the limited frame rate can be challenging to capture the ongoing subjects and EVS can be an optimal candidate.

With object counting and size estimation, the number of microscale objects with their respective sizes can be estimated during the flow. Conventional cytometry scatter plots were provided in Fig. 3.5(A), (D), (G), including the gated population of 8, 15 μm microparticles and THP-1 cells based on their sizes and granularity from FSC-A and SSC-A. For the 8 μm microparticle solution, in Table 3.1 and Fig. 3.5(B), the total event count was 3,189 with 95.6% gated for 8 μm microparticles, exhibiting a highly concentrated distribution of FSC-A measurements around 1.1 M arbitrary units, where 'M' denotes millions (i.e., 1.1M = 1,100,000) with CytoFLEX; in Fig. 3.5(C), the neuromorphic detection was adopted and generated an overall count of 3,086 with gating tolerance between ±2 μm in respective size, and yields 98.1% of the population as 8 μm microparticles. For the 15 μm microparticle solution, in

Table 3.1 – CytoFLEX and neuromorphic output on the total event count of 8 μm, 15 μm microparticles and THP-1 cells in their sample solution.

Sample name	**Total population** (CytoFLEX)	**Target population** (CytoFLEX)	**Total population** (Neuromorphic)	**Target population** (Neuromorphic)
8 μm microparticles	3,189	3,049 (95.6%)	3,086	3,027 (98.1%)
15 μm microparticles	3,220	2,990 (92.9 %)	3,898	3,848 (98.7%)
THP-1 cells	4,429	1,799 (40.6%)	3,072	N/A

Fig. 3.5(E), the total event count was 3,220 with 92.9% gated for 15 μm particles with CytoFLEX, presenting a concentrated distribution around 3.4 M in FSC-A measurement; in Fig. 3.5(F), the overall neuromorphic count was 3,898 with 98.7% gated as 15 μm microparticles. Both technologies yield remarkable counting similarities and purities in measuring pure PS beads in different sizes, constructing a highly alike size of distribution in describing the sample population. As the sample solutions are prepared with only microbeads, our strategy can compete with conventional cytometry to provide higher purity and accuracy. For THP-1 cells, in Fig. 3.5(H), a total event number of 4,429 was estimated by CytoFLEX with 40.6% identified as live THP-1 cells, 26.6% dead cells and 28.8% debris; in Fig. 3.5(I), the neuromorphic count was 3,056 and condition of the cells and division into subsets remain inaccessible owing to the inability to contrast different level of granularity. Although the majority of the ongoing objects in varied sizes can be detected, such discrepancy in the total count can be caused by the significant amount of tiny debris in the cell solution, which can be easily recognised as noise-like events during the neuromorphic flow. As a result, our platform achieved high correspondence with commercialised cytometry when conducting measurements on pure microscale objects; however, in the context of cell measurements in real practice, the debris, doublets, complexity, viability and cycle of cells can raise the parameters to be implemented to distinguish various components in cell culture.

During the early testing stage, MCF-7 cells were observed under the platform for testing the compatibility of neuromorphic vision with biological samples. In Fig. 3.3 (M),(N), in addition to the morphology acquisition, under phase contrast, the internal nucleus-like objects were identified with distinct clarity during the view without the aid of any staining techniques. Such a phenomenon can be supported by the HDR provided by neuromorphic vision. However, as this is the first instance of the event, we cannot conclude an absolute explanation on the matter. Further investigations and parallel studies on various cell lines are required to verify the specific mechanism behind it. Nevertheless, if the assumption is valid, this unique feature can contribute a deeper insight into neuromorphic cytometry and can be utilised as an additional metric in conducting cell measurement and sorting.

3.5 Conclusion

In this work, we have concluded our first milestone in performing cell population measurement in terms of object counting and size estimation. The high consistency and purity in measuring microbeads in different sizes compared to commercialised cytometry indicated the measurement accuracy and similar characterisation of neuromorphic cytometry. Although the function of classifying the cell condition and surrounding events is putting forward, the low latency and event-focused architecture in neuromorphic has the potential to outperformance the conventional IFC in throughput and data saving, enabling a prospect of a data- and cost-efficient fluorescence-sensitive high-throughput neuromorphic cytometry.

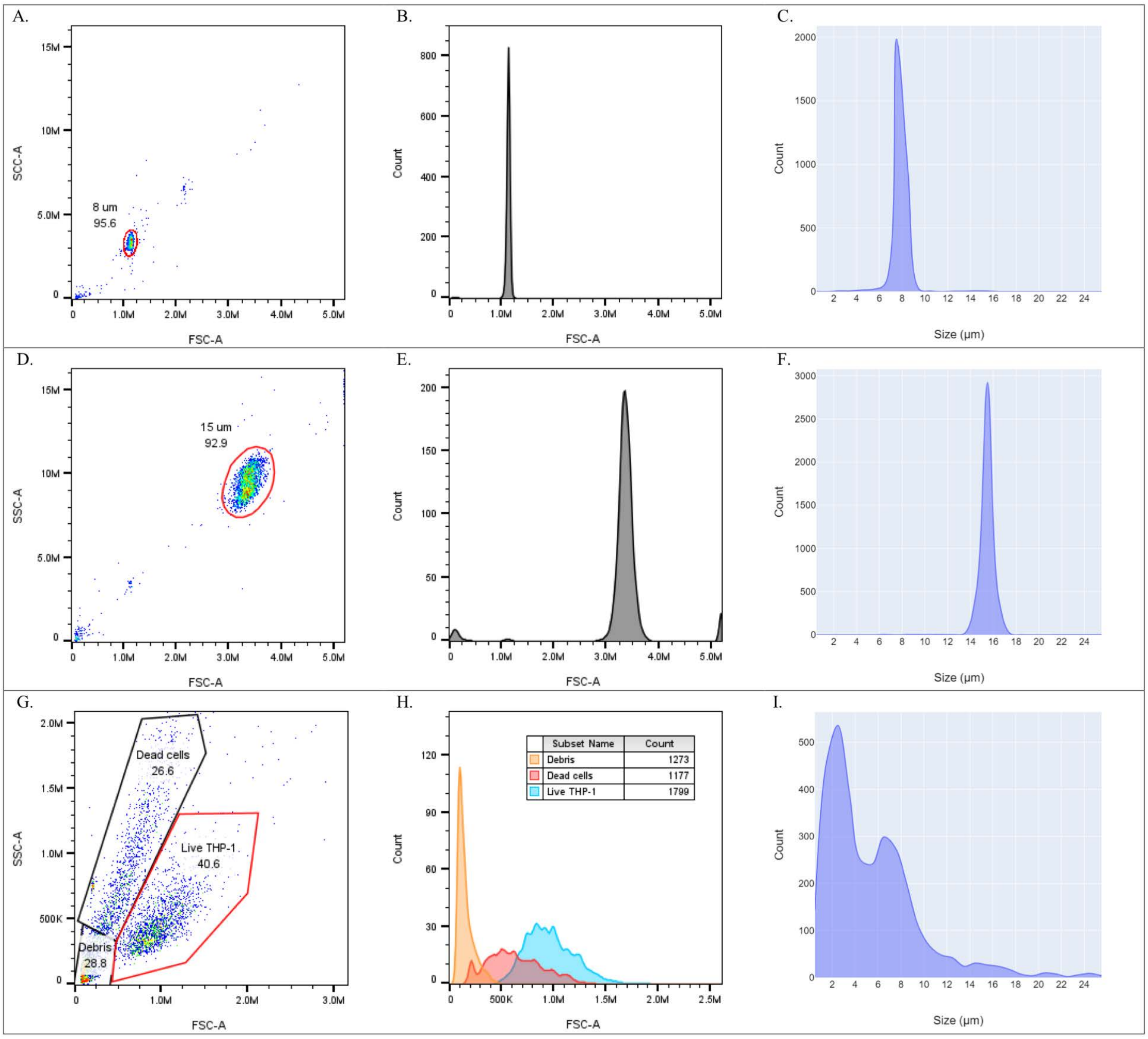

Figure 3.5 – Cytometry and neuromorphic measurements on microparticles and THP-1 cells. (A) CytoFLEX interpretation of 8 μm microparticles based on forward scatter area (FSC-A) and sideward scatter area (SSC-A), gating 95.6% of the population being 8 μm microparticles. (B) Histogram of 8 μm microparticle size distribution based on FSC-A measurement. (C) Histogram of 8 μm microparticle size distribution based on neuromorphic outputs. (D) CytoFLEX interpretation of 15 μm microparticles based on FSC-A and SSC-A, gating 92.9% of the population being 15 μm microparticles. (E) Histogram of 15 μm microparticle size distribution based on FSC-A. (F) Histogram of 15 μm microparticle size distribution based on neuromorphic outputs. (G) CytoFLEX interpretation of THP-1 cells based on FSC-A and SSC-A, gating 40.6% as live THP-1 cells, 26.6% dead cells and 28.8% debris. (H) Size distribution of live THP-1 cells, dead cells and debris based on FSC-A. (I) Histogram of THP-1 cell size distribution based on neuromorphic outputs.

Chapter 4

Cell Detection with Convolutional Spiking Neural Network

In this chapter, we advanced NIC analysis with a ML model to perform cell detection tasks on THP-1 and LL/2 cell lines, evaluating its suitability for automating manual gating strategy in working with cytometry data. The sample curated are two biological cell lines and PS particles. A SNN model was developed and trained on the curated dataset to maintain the entire framework is based on neuromorphic architecture and whether it can synergise for compatible outcomes.

- Zhang, Z., Yang, H., Eshraghian, J. K., Li, J., Yong, K.-T., Vigolo, D., McGuire, H. M., Kavehei, O. (2024). "Cell Detection with Convolutional Spiking Neural Network for Neuromorphic Cytometry." *APL Machine Learning, 2(2).* `https://doi.org/10.1063/5.0199514`

Statement of Contributions of Joint Authorship

- Ziyao Zhang (Candidate): Experimental design, project conceptualisation, experimental work, literature review, data curation, result evaluation, validation, model development, article writing, reviewing and editing.
- Haoxiang Yang: Data processing, data analysis, software programming, model development, function implementation, data visualisation, article writing, reviewing and editing.
- Jason K. Eshraghian: Expert advice on event data processing, neuromorphic operating principles, and neural network design; article reviewing and editing.
- Jiayin Li: Contributed to experimental work, data visualisation, data analysis, article reviewing and editing.
- Ken-Tye Yong: Contributed to research methods, sample selection and microfluidic design; article reviewing and editing.
- Daniele Vigolo (Co-Supervisor): Expert advice for microfluidics, flow cytometry and cell sorting; microfluidic design and fabrication; article reviewing and editing.
- Helen M. McGuire (Co-Supervisor): Expert advice on cell biology, immunology and flow cytometry; sample preparation, experimental work, data analysis, article reviewing and editing.
- Omid Kavehei (Principal Supervisor): Project conceptualisation, equipment acquisition, project administration, resources, supervision, result evaluation, validation, article writing, reviewing and editing.

In addition to the statements above, in cases where I am not the corresponding author of a published item, permission to include the published material has been granted by the corresponding author.

Ziyao Zhang Date: 22 February 2025

As supervisor for the candidature upon which this thesis is based, I can confirm that the authorship attribution statements above are correct.

Prof. Omid Kavehei Date: 22 February 2025

Manual gating in cytometry data enables the classification of discrete cell populations based on extracted features. However, this expert-driven technique can be subjective and laborious, often presenting challenges in reproducibility and being inherently limited to bivariate analysis. Numerous AI-driven cell classifications have recently emerged to automate the process of including multivariate data with enhanced reproducibility and accuracy. The previous chapters demonstrated the early development of NIC, evaluating its feasibility in addressing the limitations of conventional frame-based imaging systems in fluorescence sensitivity and throughput. Herein, we trained a SNN-YOLO model to perform cell classification and detection on label-free samples under neuromorphic vision. Spiking techniques are inherently suitable post-processing techniques for neuromorphic vision sensing. The experiment was conducted with PS-based microparticles, THP-1, and LL/2 cell lines. The network's performance was compared to a traditional YOLOv3 model fed with event-generated frame data to serve as a baseline. In this work, our SNN-YOLO outperformed the YOLOv3 baseline by achieving the highest average class accuracy of 0.974, compared to 0.962 for YOLOv3. Both models reported comparable performances across other key metrics and should be further explored for future auto-gating strategies and cytometry applications.

4.1 Introduction

Manual gating is adopted with IFC data to distinguish cells into discrete populations based on cell measurement. In IFC, 2D scatter plots are distributed based on measured cell characteristics, often combining morphological-related parameters with assigned fluorescence signals (Lippeveld et al., 2019). Although this strategy can effectively isolate the populations of interest, manual operation can lead to numerous challenges, especially with high-dimensional cytometry data, as the following:

(1) A gating technique requires an experienced researcher or expert to correctly interpret the morphological and fluorescence data to isolate the populations.

(2) Manual gating of the high-dimensional cytometry data can inhibit the interpretation into a bivariate hierarchical analysis of 2D scatter plots. In comparison, IFC was designed to offer multivariate spatial feedback to reveal more intricate and insightful data structures.

(3) This expert-driven process may need to be applied repeatedly based on experiment and sample variety, which can generate a laborious workload for large experiments.

(4) The interpretation can be subjectively biased and challenging to reproduce.

(5) Multiple fluorescence tags are often paired during cell readout and gating; this can be cost-expensive and inflict confounding effects on the cells under research (Hu et al., 2022; Lippeveld et al., 2019).

Thus, an automated gating strategy with label-free subjects is warranted to overcome these drawbacks, enhancing IFC cell workflow and insights. Many endeavours have been established to annotate cell populations with ML models as well as to discover rare cell events from the high-dimensional data (Arvaniti and Claassen, 2017; Cheng et al., 2022; Hu et al., 2022, 2020; Qiu et al., 2011).

Neuromorphic vision sensors NVS can asynchronously fire individual pixels to transmit only the active pixel's array address according to the contrast changes in a scene. This event-focused architecture enables data efficiency, low latency, high temporal resolution, and low-light sensitivity (Lichtsteiner et al., 2008; Mueggler et al., 2017). Our previous attempt at NIC proposed that these unique characteristics of NVS can be a promising candidate for handling cell events in a high-throughput, data-efficient, and fluorescence-sensitive manner. We evaluated the feasibility of exploiting such a vision to conduct cytometric-like functions and accomplished high consistency with a commercially available flow cytometer, CytoFLEX (Zhang et al., 2023). Building upon NIC work, we adopted a ML approach to automate the basic cell analysis. In detail, a convolutional SNN combined with the YOLOv3 model SNN-YOLO was developed to perform cell classification and detection on label-free microscale objects. This work also assesses the compatibility of neural networks and imaging techniques under neuromorphic architecture in measuring cell events. The experiment was carried out with 3, 8, 15 μm PS-based microparticles, THP-1, and LL/2 cells. In addition, to validate the accuracy of our model, the baseline performance of a traditional YOLOv3 fed with event-generated frames was included.

4.2 Related work

Convolutional Neural Network (CNN)s are a deep learning model designed to adaptively learn spatial hierarchies of features from low- to high-level patterns, accomplishing remarkable performance for processing data with a grid pattern, including images (Yamashita et al., 2018). Recent efforts have been investigated to develop an AI-driven cell classifier that can categorize cell identities based on the measured features. Research conducted by Eulenberg et al. (2017) develops a CNN, DeepFlow, to reconstruct the cell cycle of Jurkat cells in seven different stages, including interphases of G1, S, G2 and mitosis phases of Prophase, Anaphase, Metaphase, Telophase, reporting accuracy of 0.794 when considered seven phases with their respective class, and an accuracy of 0.987 by categorising G1, S, and G2 phases as a single class. In addition, Lippeveld et al. (2019) utilized CNNs, ResNet, and DeepFlow to classify the white blood cell dataset, reporting a balanced accuracy of 0.649 and 0.703. The models were also adopted to classify the eosinophil dataset with activating and resting states, contributing a balanced accuracy of 0.831 and 0.871. All these endeavours and their proven contributions encourage the automation of sample gating with ML to alleviate the cumbersome workload and manual featuring.

In this work, we exploited a YOLOv3 variant with a modified backbone module based on the Energy-efficient Membrane-Shortcut Residual Network (EMS-ResNet) developed by Su et al. (2023) to train the SNN directly. The modified module comprises a convolutional layer, BNTT, and Leaky Integrate-and-Fire (LIF) neurons in SNN to convert extracted features into time-sequential data. The backbone model was combined with a detection head, YOLOv3, for cell classification and detection. Adopting

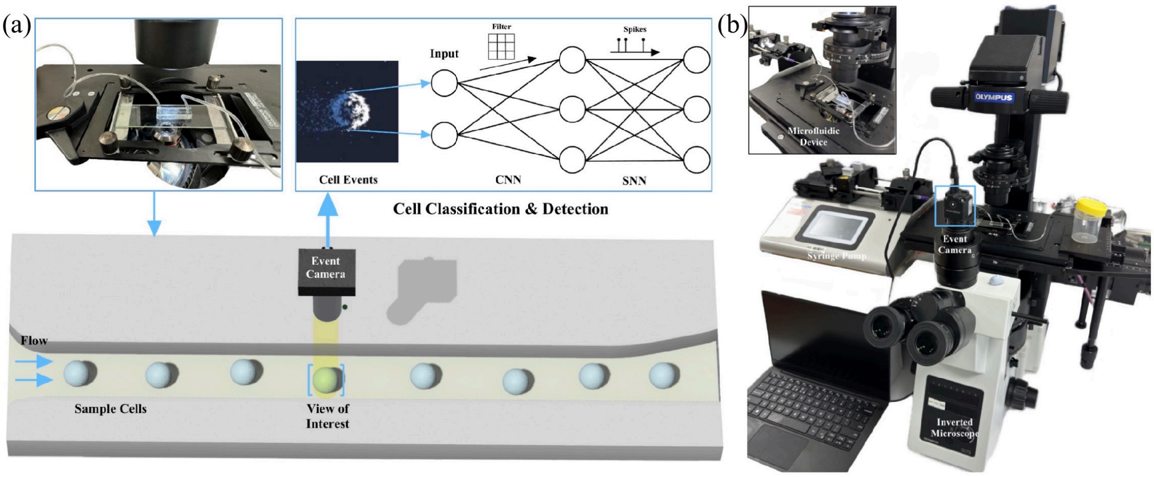

Figure 4.1 – Illustrative schema of neuromorphic imaging cytometry: (a) The sample cells were introduced into the microfluidic channel, and the event camera captured physical characteristics. The cell events were imported into the SNN-YOLO model for cell classification and detection. (b) The configuration of the platform with the event camera mounted onto the inverted microscope and connected to a computer for imaging collection.

a spatiotemporal architecture in imaging collection and deep learning can inspire an event-dedicated, data-efficient, high-throughput paradigm for future cytometry and gating applications.

4.3 Methodology

4.3.1 Sample Preparation

PS-based microparticles in the size of 3, 8, and 15 μm at a concentration of 10 wt.% (Sigma-Aldrich, USA) were used to simulate cells with different volumes. Particles were diluted with PBS supplemented with 0.1% Triton X-100 into a final concentration of 1×10^5 particles/mL. This procedure ensured an adequate sample count while maintaining sufficient spaces among particles, preventing particle aggregation or adherence to the delivery channel.

A human leukemia monocytic cell line, THP-1 cells were cultured with RPMI 1640 medium supplemented with 10% fetal bovine serum, 2mM L-glutamine, 100U/mL

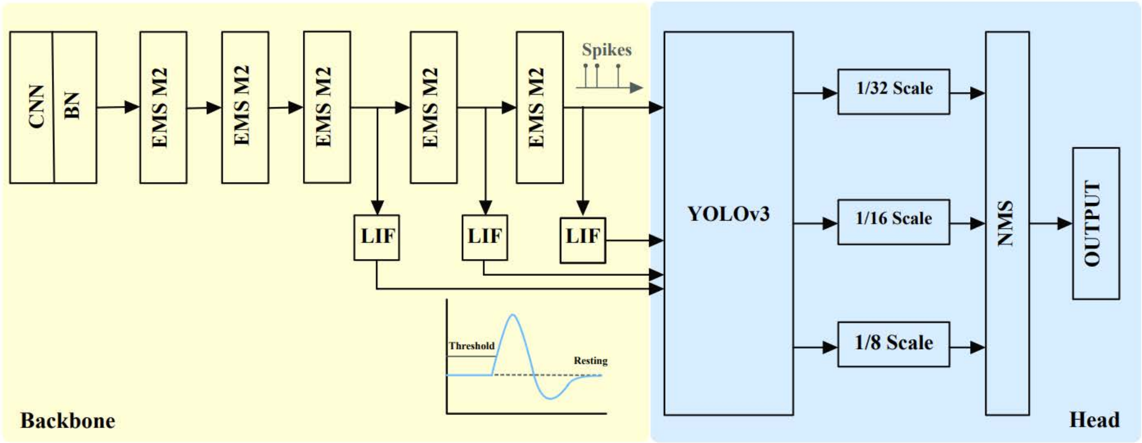

Figure 4.2 – The architecture of the SNN-YOLO network. The backbone comprises a convolutional layer, BNTT, and EMS Module2 for feature extraction. The detection head adopted a traditional YOLOv3 model to classify and detect objects.

penicillin, and 100 μg/mL streptomycin. The cell line was collected and centrifuged at a speed of 400g for 5 minutes. The cell pellet was retrieved and re-suspended with a flow cytometry buffer made of 0.02% sodium azide, 0.5% BSA, and 2mM EDTA in PBS. The dilution was applied during the re-suspension to reach a final concentration of 1×10^5 cells/mL. The sample solution was vortexed and equally distributed into aliquots for microfluidic delivery and cell classification under neuromorphic vision.

A murine Lewis lung carcinoma cell line, LL/2 cells were maintained with Dulbecco's Modified Eagle's Medium (DMEM) supplemented with 10% fetal bovine serum. The sample was harvested and centrifuged at 200 g for 5 minutes. The cell pellet was collected and re-suspended with the flow cytometry buffer. The dilution was conducted during the re-suspension into a final concentration of 1×10^5 cells/mL. The solution was then vortexed and equally aliquoted before the delivery procedure.

4.3.2 Microfluidic Imaging Platform

A straight microfluidic channel (35 μm-height, 100 μm-width and 30 mm long) was fabricated out of Polydimethylsiloxane (PDMS) (Sylgard® 184 Silicone Elastomer Kit, Dow Corning, UK), utilizing a standard soft-lithography protocol (Zaouk et al., 2006). The narrow height of the channel was designed to restrain the position of the particles, aligning them into a relatively limited plane for in-focus imaging. A neuromorphic camera, EVK4 (Prophesee, France), operated at 1280 × 720 resolution, 4.86 × 4.86 μm pixel size with time resolution equivalent to $> 10,000$ fps, was mounted on an inverted microscope (IX73 Inverted Microscope, Olympus, Japan). The camera recorded the dynamics at the center of the channel using a 20× magnification objective. Phase contrast was also adopted to enhance the contrast of the cell samples.

Each sample solution was loaded into a 1mL syringe (Terumo Syringe, Terumo Corporation, Philippines) and introduced into the microfluidic channel via a syringe pump (LEGATO 200 Syringe Pumps, KD Scientific Inc, USA) operating at the flow rate of 1μL/min. After each delivery class, a new channel was adopted to avoid contamination of the collected data by the leftover particles. A reduced flow rate was adopted in this experiment to increase the exposure time permitted to the sensor under the neuromorphic vision. The constant flow in the channel induced the necessary light changes between the particles and the background, activating the correlated pixels to represent the cell events. Once the objects travelled through the field of view, the event camera recorded all dynamics in the scene. Metavision Studio software provided by Prophesee was used during the recording to optimize the visual feedback with adjustable accumulation time and event-generated threshold. A 60-second footage was recorded three times per object class. A total of 900 seconds of event footage was collected to train the SNN-YOLO network.

4.3.3 Data Preprocessing

Particles of different sizes as well as THP-1 and LL/2 cells were verified by the cell researcher at the Charles Perkins Centre, University of Sydney. The researcher has expertise in cell research with an advanced background in the analysis of microscale objects under microscopic and neuromorphic vision. The data were annotated by the individual following the You Only Look Once (YOLO) formatting standards, considering the sample sizes, morphological information, methods of culture, and nature of the cell lines. This approach ensured that a high degree of accuracy and reliability was maintained in the annotated dataset.

For data preprocessing, the resolution was reduced via the four-step preprocessing implementations (Abreu et al., 2023). The event visualisation window was cropped into a 10% width area at the sensor's centre and the event coordinates were down-sampled with a scaling factor of four. The pre-processed event stream was integrated into a layer of LIF neurons. A filtering technique was applied to eliminate random noise by setting the $V_{\text{th}} = 3.5V$, which required more continuous events to trigger a single spike from a neuron. The data were separated into individual samples with a duration time of 200 μs. Within the sample, each event was allocated to four different time bins. To remove the samples without any particles, the samples containing fewer than 150 events were discarded.

We mapped 2D representations from the event stream at fixed temporal bins for the data labelling. A labelling tool, LabelImg (Tzutalin, USA), was utilised to annotate all the particles that existed in the sample.

4.3.4 Convolutional SNN Development

In this work, we adopted a directly trained SNN object detection network, inspired by Energy-efficient Membrane-Shortcut You Only Look Once (EMS-YOLO) previously proposed by Su et al. (2023), and the original YOLOv3 network for object detection and classification tasks. These models mainly consist of two modules: a feature extraction backbone and a detection head.

In the backbone, we implemented the SNN residual blocks, Membrane-Shortcut (MS)-Block and EMS-Block, to replace the similar function block in the YOLOv3 backbone (DarkNet-53). These two residual blocks enabled a deeper network's depth without causing gradient vanishing.

- The MS-Block was structured with two sequentially connected LCB blocks. The LCB comprised sequentially connected layers: a LIF layer, a convolution layer, and a batch normalisation layer with a residual connection.

- The EMS-Modules had two branches: the first had two connected LCB blocks; the second started with a max pooling layer to increase channel numbers. A split path was followed with one connection to the LCB block and a shortcut path. All outputs were concatenated into one output, combined with the first branch's output.

To process the time series data in the event stream, a temporal BNTT was applied to the network, enabling it to effectively normalise the features across both spatial and temporal dimensions (Kim and Panda, 2021). The membrane potential activities of this layer can be represented by Equation 4.1 (Eshraghian et al., 2023a):

$$U_i^t = \lambda u_i^{t-1} + \mathrm{BNTT}_{y_t} = \lambda u_i^{t-1} + \gamma_i^t \left(\frac{\sum_j w_{ij} S_j^t - \mu_i^t}{\sqrt{(\sigma_i^t)^2 + \epsilon}} \right) \tag{4.1}$$

where λ is the leak factor and γ_i is a learnable parameter whose value changes over time. Both parameters range from (0, 1); w_{ij} represents each spike's weight between two neurons. S_j^t is the binary spike at t timestep which are expressed by volts (V), $\sigma(V)$ is the global variation and $\mu(V)$ is the global mean.

This approach ensures consistent internal network dynamics over time, which is critical for maintaining stability and improving learning efficiency in networks processing temporal data. Moreover, object detection is a hybrid task that combines classification and regression. SNN models have difficulties in regression tasks because of the binary input data. To address this problem, we added potential-assisted blocks, a LIF block proposed in Zhu et al. (2022), to the SNN network. Following the approach, we introduced three membrane potential neuron layers at the network's downsampling stages. The outputs of these layers were concatenated with the final membrane potential in the output layers to produce the prediction area.

In the training of SNNs, the Surrogate Gradient algorithm (Eshraghian et al., 2023a; Fang et al., 2021) plays a pivotal role in facilitating the learning process, despite the inherently non-differentiable nature of spiking neurons. The algorithm employs a continuous approximation of the network's discrete spiking behaviour, which can be shown in Equation 4.2, allowing for the application of gradient-based optimisation methods.

$$S \approx \tilde{S} = \frac{1}{\pi} \arctan\left(\pi U - \frac{\alpha}{2}\right) \tag{4.2}$$

where U is the membrane potential, and α is a parameter that defaults to two.

Therefore, by integrating the Surrogate Gradient algorithm(Eshraghian et al., 2023a; Fang et al., 2021) and the algorithm of AdamW optimizer(Loshchilov and Hutter, 2019), the parameter update process during the model training can be represented in Equation 4.3, 4.4:

$$\nabla_w \approx \sum_t \sum_{s \leq t} \frac{\partial \tilde{S}}{\partial U} = \sum_t \sum_{s \leq t} \frac{1}{\pi} \left(\frac{1}{1 + \left(\pi U^{\frac{\alpha}{2}}\right)^2} \right) \tag{4.3}$$

$$w_{t+1} = w_t - \eta \cdot \left(\frac{\hat{m}_t}{\sqrt{\hat{v}_t} + \epsilon} + \lambda w_t \right) \tag{4.4}$$

where $\hat{m}_t$ is the bias-corrected first-order moment estimates of gradients (∇_w), $\hat{v}_t$ is the bias-corrected second-order moment estimates of gradients, and both of them are the function of gradients. η is learning rate, and λ is the weight decay.

In the detection module, a conventional YOLOv3 was adopted to perform object detection, enabling three different scales to figure out objects of various sizes (Farhadi and Redmon, 2018). Our SNN network was constructed using snnTorch developed by Eshraghian et al. (2023a). The model was trained with the dataset for 150 epochs with an AdamW optimiser(Loshchilov and Hutter, 2019) to enhance generalisation performance. We used 3×10^{-5} and 1×10^{-4} for the learning rate (η) and weight decay (λ) in Equation 4.4. All training sessions were conducted on a machine equipped with 64GB Random Access Memory (RAM), a 14-core Intel i5-13600kf Central Processing Unit (CPU), and an RTX2080Ti Graphics Processing Unit (GPU) with 11 GB VRAM.

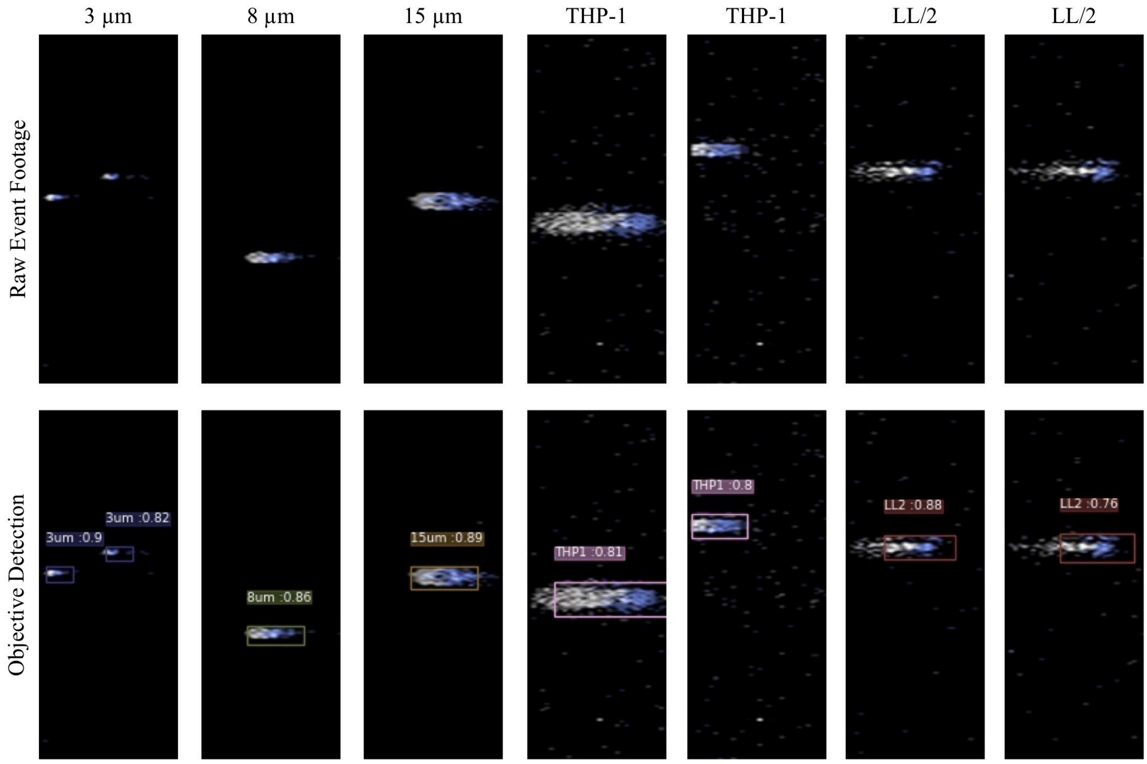

Figure 4.3 – The raw event footage of 3, 8, 15 μm microparticles, THP-1 and LL/2 cell lines in contrast to event footage processed by the SNN-YOLO with bounding boxes representing categorized class and class confidence.

4.4 Results and Discussion

The configuration of the current NIC setting was demonstrated in Fig. 4.1. Cells were introduced into the microfluidic channel with a constant flow rate. The channel was designed with a narrow height of 35 μm to restrain the vertical position of the particles, reducing the impacts of poor imaging quality caused by out-of-focus particles. The reduction in height can also alleviate the extensive calibration required for in-focus imaging. Moreover, as a decreased height was integrated into the experiment, the number of particles should be carefully addressed to avoid channel blockage. The integrated NVS captured the physical characteristics of the samples at a 20× magnification to enhance the morphological details, attempting to increase more distinct features among cell types. The collected footage was trained on the SNN-YOLO network to perform cell classification and detection tasks. Depending

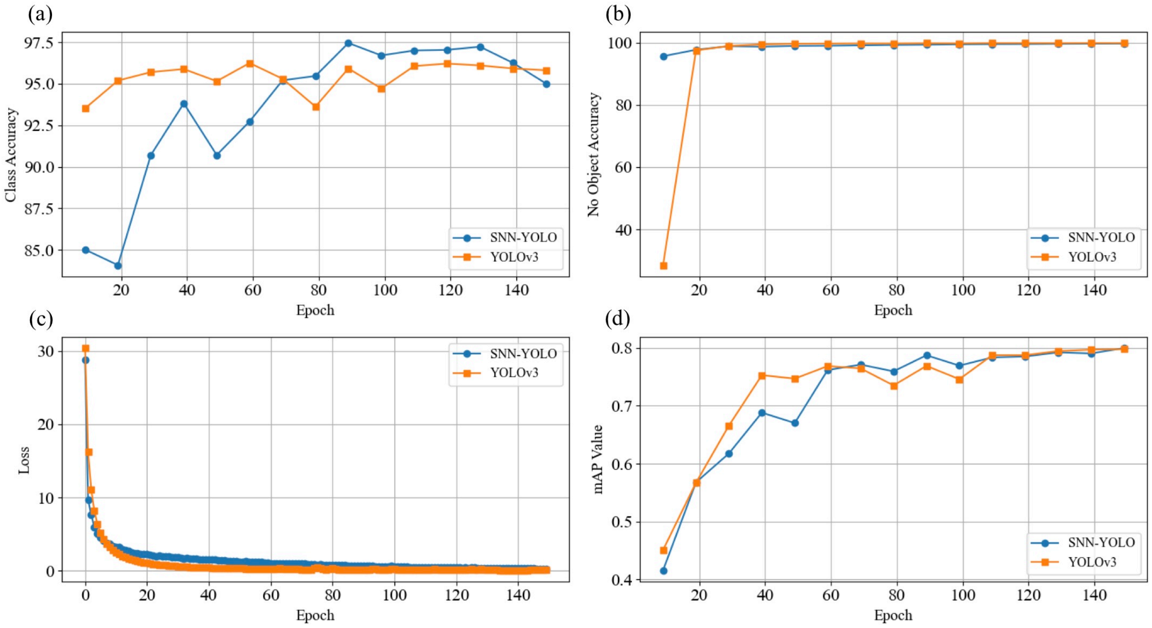

Figure 4.4 – Recorded training curves for the SNN-YOLO and YOLOv3: (a) Average class accuracy during the training process for every 10 epochs. (b) Average no-object accuracy for every 10 epochs. (c) Average loss during the training process for every epoch. (d) Average mAP during the training process for every 10 epochs.

on future endeavours, the platform can implement an inertial microfluidic focusing technique to align the particles into a common travelling path vertically and horizontally (Di Carlo, 2009). This can significantly reduce the risks and limitations of the technique, optimising the permitted throughput and data quality per experiment. Furthermore, if real-time classification decisions are available, the trained model and the platform in this research can integrate into a cell-sorting device to isolate or collect the cells of interest from a large population.

The architecture of the SNN-YOLO model was demonstrated in Fig. 4.2. The 2D representation based on temporal bins of the event stream was fed to the model for feature extraction, direct SNN training, classification, and detection purposes. Input events were first imported to the feature extraction backbone. A convolutional layer transformed inputs into corresponding spikes, and temporal BNTT normalised the extracted features into spatial and temporal dimensions. The following EMS-Module2 contained LIF neurons to integrate input spikes and output firing was triggered once the signal accumulation surpassed the threshold. For the detection head, a conven-

Table 4.1 – SNN-YOLO and YOLOv3 performance accuracy percentage (%) and mAP of each class for every 50 epochs.

TYPE	**Epoch**	**mAP@50***	**3 μm**	**8 μm**	**15 μm**	**LL/2**	**THP-1**
SNN-YOLO	50	0.670	0.960	0.933	0.816	0.669	0.992
SNN-YOLO	100	0.769	0.995	0.999	0.926	0.900	0.984
SNN-YOLO	150	0.799	0.997	0.999	0.926	0.767	0.984
YOLOv3	50	0.747	0.997	0.979	0.965	0.864	0.923
YOLOv3	100	0.746	0.975	0.965	0.979	0.885	0.936
YOLOv3	150	0.798	0.997	0.986	0.993	0.853	0.944

tional YOLOv3 model was adopted to perform classification and track the position of the objects from the given event stream by considering three different scales to verify objects of various sizes. In the work of Su et al. (2023), the EMS-YOLO was based on the YOLOv3-tiny framework, which limited the network to two scales of predictions and could not perform multiple size realisation. Thus, we adopted a modified Darknet-53 with a YOLOv3 framework to conduct the detection tasks.

The SNN-YOLO model was trained on a five-class dataset. The raw event footage of 3, 8, 15 μm microparticles, THP-1, and LL/2 cells under 200 μs accumulation time was illustrated in Fig. 4.3. After being processed by the network, the object of interest was marked by a bounding box to represent the object's coordinates, categorised class, and class confidence.

The model performed multi-target detection, demonstrated with 3μm particles in the scene. However, as this experiment used a relatively narrow channel and the view of interest was divided into 10% width of the original vision, the chance of collecting multiple large targets in a common scene was rare. In Table 4.1, the average accuracy and mAP for every 50 epochs of the SNN-YOLO and YOLOv3 were reported for each class. Both models classified and detected the microscale targets with a high accuracy rate, except for LL/2 detection with optimal accuracy of 0.900 and 0.885 for SNN-YOLO and YOLOv3 at 100 epochs. The underperformance could be attributed to the incomplete pixel-address registration of morphological data by the universal accumulation time and optical setup applied to all samples. As objects in the channel could move at different velocities and depths, the visual representation of certain cell events might be compromised by a constant value, especially considering the complexity of cell structures. Additionally, a noticeable reduction in LL/2 accuracy was observed in both SNN-YOLO and YOLOv3, dropping from 0.900 and 0.885 at 100 epochs to 0.767 and 0.853 at 150 epochs. This decline suggests that the model may have overfitted during extended training with the LL/2 dataset and could also result from learning compromised features. Even though this study adopted a channel with reduced height to limit the travelling plane, the free space still existed, and a further decrease in the dimensions could cause particle aggregation and channel blockage. For future endeavours, a focusing technique should be incorporated to unify the objects in motion into a common pathway, enhancing the visual integrity of the cells under neuromorphic vision.

The highest score of SNN-YOLO was 0.999 in detecting 8 μm particles, and YOLOv3 achieved 0.997 for 3 μm particles. Both models acquired highly similar mAP values (0.799 and 0.798) after 150 epochs. The training curve of average class accuracy, no-object accuracy, loss, and mAP values for every 10 epochs was illustrated in Fig. 4.4. In average class accuracy, the YOLOv3 started with a high accuracy rate of 0.952 at 20 epochs and reached its highest of 0.962 at 60 epochs. Even though the training requirement to achieve the desired outcome was realised sooner by YOLOv3, the SNN-YOLO demonstrated an increase in accuracy, starting from 0.841 at 20 epochs and outperforming YOLOv3 after 70 epochs, resulting in the highest average accuracy score of 0.974 at 90 epochs. Additionally, SNN-YOLO attained high no-object accuracy in a brief period of the training process compared to YOLOv3. Regarding loss and average mAP, both models coherently descended and ascended as the number of epochs increased.

In this study, we successfully trained a convolutional SNN with the YOLO model to conduct cell detection and outperform a conventional YOLOv3 in terms of average accuracy score (0.974 *vs.* 0.962). Although both models exhibited comparable performance across other key metrics, the SNN network has been indicated as a preferred neural network in working with neuromorphic architecture (Kim et al., 2020). Considering the superior energy efficiency and real-time processing of SNN, combining SNN with NVS data can significantly benefit any time-sensitive or point-of-care cell tasks, such as microfluidic cell sorting. For future endeavours, an increase in data categories of cell types should be involved to reveal the key features in individual cells. One of the long-standing challenges in label-free cell classification is sub-typing cells with similar morphological structures (Eulenberg et al., 2017; Lippeveld et al., 2019). In this case, differentiating more vital or subtle features is essential to classify them correctly. Moreover, optimisation of the current NIC platform can enable numerous applications and high-performance outcomes. These bio-inspired machine learning and imaging approaches can be promising candidates for next-generation auto-gating and cytometry applications.

4.5 Data Availability

The code that supported this article is available at `https://github.com/NeuroSyd/SNN-YOLO-Cell-Detection`. Additional data is available from the corresponding authors upon request.

Chapter 5

Classification and Cell Analysis of Human Blood Cells

In this chapter, we utilised our platform to experiment with more clinically practical and complicated cells from human blood samples, curating the first neuromorphic cell dataset with the detailed resolution provided. We also developed a lightweight hybrid SNN model to perform cell classification and analysis for six classes of samples, including RBCs, neutrophils, lymphocytes, platelets, PS particles and HUVECs. In this section, we included our latest and more comprehensive insights on NIC and IFC compared to our initial proposal.

- Zhang, Z., Yang, H., Li, J., Chong, S. W., Eshraghian, J. K., Yong, K.-T., Vigolo, D., McGuire, H. M., & Kavehei, O. (2024). "Neuromorphic Imaging Cytometry on Human Blood Cells." *bioRxiv*, 2024–11. Cold Spring Harbor Laboratory. `https://doi.org/10.1101/2024.11.16.623904`

Statement of Contributions of Joint Authorship

- Ziyao Zhang (Candidate): Experimental design, project conceptualisation, experimental work, literature review, data curation, result evaluation, validation, model development, manuscript writing, reviewing and editing.

- Haoxiang Yang: Data preprocessing, data analysis, software programming, model development, function implementation, data visualisation, manuscript writing, reviewing and editing.

- Jiayin Li: Experimental work, data visualisation, data analysis, manuscript reviewing and editing.

- Shin Wei Chong: Sample preparation, experimental work, visualisation, manuscript reviewing and editing.

- Jason K. Eshraghian: Expert advice on event data processing, neuromorphic operating principles, and neural network design; manuscript reviewing and editing.

- Ken-Tye Yong: Contributed to research methods, sample selection and microfluidic design; manuscript reviewing and editing.

- Daniele Vigolo (Co-Supervisor): Expert advice for microfluidics, flow cytometry and cell sorting; microfluidic design and fabrication; manuscript reviewing and editing.

- Helen M. McGuire (Co-Supervisor): Expert advice on cell biology, immunology and flow cytometry; sample preparation, experimental work, data analysis, manuscript reviewing and editing.

- Omid Kavehei (Principal Supervisor): Project conceptualisation, equipment acquisition, project administration, resources, supervision, result evaluation, validation, manuscript writing, reviewing and editing.

In addition to the statements above, in cases where I am not the corresponding author of a published item, permission to include the published material has been granted by the corresponding author.

Ziyao Zhang Date: 22 February 2025

As supervisor for the candidature upon which this thesis is based, I can confirm that the authorship attribution statements above are correct.

Prof. Omid Kavehei Date: 22 February 2025

Recently, numerous endeavours have been invested to develop NIC with diverse modalities and ML approaches to overcome the traditional constraints of IFC. However, the majority of the current investigation is focusing on artificial particles instead of biological cells, which fails to capture the intricate and meaningful biological structure of cells. In this work, we adopted our NIC to experiment with clinically significant cells from human blood samples, curating the first neuromorphic cell dataset with RBCs, neutrophils, lymphocytes, platelets, PS particles and HUVECs. Such a dataset serves as a baseline of healthy cell groups for future diagnostic and research purposes. In addition, the rich spatial information derived from cell images has exceptional uses with Deep Learning (DL) approaches to automate cell analysis, classification, sorting, and gating strategy. We trained a lightweight model combining the convolutional block attention module with a spiking neural network, CBAM-SNN to automate cell analysis and classification. The proposed architecture has achieved a promising performance of 97% accuracy and F1 score with a significant reduction in computation requirements. Combining the data sparsity in neuromorphic imaging with a lightweight DL model and operation platform can enable next-generation, AI-driven cytometry to deliver point-of-care diagnostic and research solutions.

5.1 Introduction

The morphological information of cells serves as gold criteria for disease diagnosis and prognosis (Salek et al., 2023; Salto-Tellez, 2018). Cell morphology, structure and composition are closely linked to their physiological function and are crucial for cell identity (Caicedo et al., 2017; Nitta et al., 2018). IFC is an indispensable cell analytic tool that measures cells with rich spatial and fluorescence information from single-cell images, characterising cells with high-dimensional multi-parameters (Barteneva et al., 2012; Rees et al., 2022). IFC offers visualisation conventionally by FBSs, such as CCD or CMOS, to capture cells in a flow stream (Han et al., 2016; LaBelle et al., 2021; Rees et al., 2022). As with any image-enabled instrumentation, IFC is also susceptible to the triangle of imaging constraints—speed, resolution, and sensitivity;

increasing one performance can lead to degradation in others (Rees et al., 2022). Furthermore, characterising cells with frame-based architecture can accumulate enormous pixel data registered with blank and redundant background information that is irrelevant to cell events. Such data structures can generate a significant data volume and are cumbersome for real-time processing, especially considering the concentration of a cell population can easily exceed 1×10^6, cells/mL and multiple tests may be required for one experiment. With the ImageStream system, a sample concentration of 2–3 $\times 10^7$, cells/mL is recommended for operation (Rees et al., 2022). Thus, a data-efficient image acquisition system with high temporal resolution remains untapped for resolving the conventional constraints of IFC.

In the previous chapters, we have discussed our development of a NIC to resolve the conventional challenges in IFC. Recently, this paradigm has emerged in diverse modalities and ML methods. Abreu et al. (2023) implemented an SNN on neuromorphic hardware to enable fast and energy-efficient binary particle classification for 16μm and 20 μm PMMA microspheres, achieving 98.5% accuracy with an event-based pipeline and 97.5% with frame-based data. The following work by Gouda et al. (2024a) on fungal cells and PMMA microparticle classification using both unsupervised and supervised learning techniques, including K-means, PCA, and logistic regression, attaining 100% accuracy with PCA without relying on training annotations. In addition, the recent work conducted by Tsilikas et al. (2024)developed an NIC integrated with lightweight photonic neuromorphic processing, achieving high classification accuracy for 12 μm, 16 μm, and 20 μm PMMA particles while significantly reducing the number of trainable parameters. The proposed architecture reported a classification accuracy of 98.2% and 98.6% for the optimal FNN and RNN configurations. At the current stage, the majority of the research is experimenting with artificial-made particles instead of biological cells or experimenting with extremely limited biological classes (one or two) without providing detailed and subcellular resolution. This can lead two major concerns that need to be addressed: (1) one of the core motivations for developing an image-enabled cytometer is to visualise cells with spatial resolution on cell morphology, subcellular structure and localisation. A NIC platform without this capacity will lose the key advantage of being an image-enabled system. (2) in the ML aspect, training a model with limited biological classes and simple morphological structure can make the model fail to learn the complicated and subtle phenotypical expression of cells. This can render the algorithm incapable of being generalised for broader cell events or clinical uses, especially for the use of a cytometer.

In this work, we utilised our NIC to curate a label-free neuromorphic cell dataset, including human blood cells (RBCs, neutrophils, lymphocytes, platelets), primary HUVECs, and PS-based microparticles with well-defined morphology. The structural integrity, cell counts, and characterisation of human blood cells serve as diagnostic criteria for many critical conditions such as sickle cell anaemia, leukaemia, sepsis, and blood cancer (Alsalem et al., 2018; Alzubaidi et al., 2020; Boldú et al., 2021; Sant et al., 2010; Sen et al., 2021; Young et al., 2021). Although this dataset does not include cells with abnormalities, it can demonstrate a standard baseline for the healthy cell group to compare with diseased cells. Moreover, the presence of circulating endothelial cells is a rare event in peripheral circulation. The increased numbers can indicate vascular injury, vasculogenic stimuli, or other disease states (Blann et al., 2005; Khan et al., 2005; Samsel et al., 2013). To the best of our knowledge, none of the preceding studies has demonstrated biological cells captured by NVS in detail and whether it is capable of depicting informative features under such a unique perception. With the continuous emergence and development of neuromorphic-enabled cytometry and cell analysis, this dataset is pivotal for future work in NIC. Furthermore, we have directly trained a lightweight hybrid model, CBAM-SNN, to automate cell feature analysis and classification tasks. This model has accomplished a 97% accuracy and F1 score with a significant reduction in memory usage and power consumption compared to a classic CNN. With the short inference time and advanced accuracy, this approach also holds great promise for enabling high-throughput image-based cell sorting (ICS) or other applications requiring fast intervention on sample cells. Combining the data sparsity in neuromorphic imaging with a lightweight DL model and operation platform can enable next-generation, AI-driven cytometry to deliver point-of-care diagnostic and research solutions.

5.2 Results & Discussion

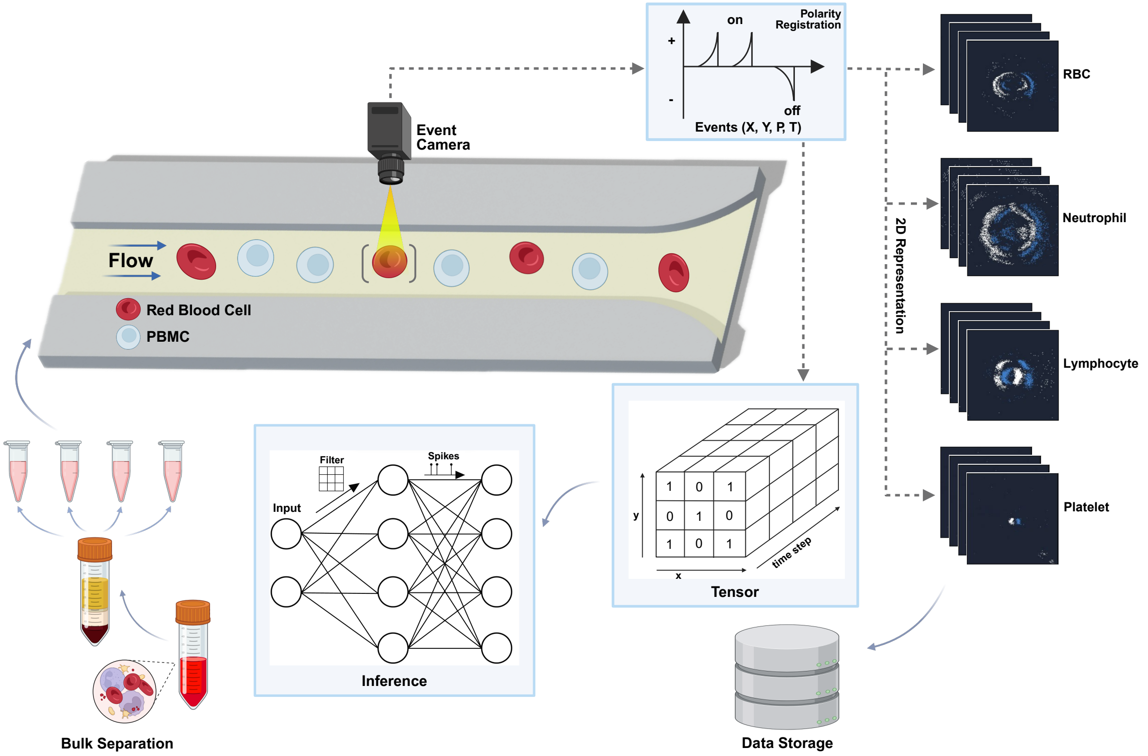

Figure 5.1 – Schema of the neuromorphic imaging platform. The samples were prepared by bulk separation to extract the cells of interest. As the cells were introduced into the microfluidic channel, the cell events were registered by NVS for two usages: **(1)** cell events were transformed into 2D images for visualisation and data curation. **(2)** cell events were transformed into tensors that undergo a neural network for cell classification.

5.2.1 Neuromorphic imaging platform

Human blood samples and other sample cells undergo bulk separation to obtain targeted cell lines. Cells are introduced into NIC, as shown in Fig. 5.1. As the cells pass through the view of interest, an NVS records the cell features with their respective pixel address, polarity and timestamp (x, y, p, t). Such information can be divided into two usages: **(1)** collected events are transformed into tensors and then inferred by the developed CBAM-SNN to conclude its respective class. **(2)** events are transformed into frame-based outputs to examine the integrity of captured features and allow calibration work to optimise the visual effects. These data are then curated into the dataset for further analysis and model development.

5.2.2 Data curation

RBCs, neutrophils, lymphocytes, platelets, HUVECs, and 8 μm particles were curated in an event format and image format at a resolution of 224 ×224 pixels for illustration in Fig. 5.2. Cell images containing multiple targets were included for enhanced generalisation and robustness. 8 μm particles were added to resemble similar sizes of RBCs and lymphocytes to potentially increase the data complexity and constrain the model for low-dimensional feature extraction based only on size variants.

The average number of activated pixels of each class under neuromorphic vision was recorded and compared with the frame data. Owing to the sparse activation in NVS, cells were registered only with correlated pixel addresses, whereas frame data contain a fixed pixel quantity regarding the default resolution, resulting in a significant difference in overall pixel recruitment. This difference can be exacerbated when observing particles of smaller sizes, as these objects only require a small proportion of pixels to characterise themselves. In this dataset, pixel activation in NVS has a 15–240 times reduction compared to the frame data.

The total number of collected cell images is also illustrated in Fig. 5.2. The discrepancy in cell images curated for each sample type can be due to the natural concentration difference in samples, loss during microfluidic delivery, and the separation yields. Furthermore, the ± polarity of NVS data is based on contrast changes. Objects travelling in various directions can lead to distinct changes in colour distribution. To encompass a broader perspective of cells, we rotated each image at a 90-degree angle three times and generated a new cell image at each rotation. This augmentation technique can enhance the model to become invariant to orientation and expand the data volume.

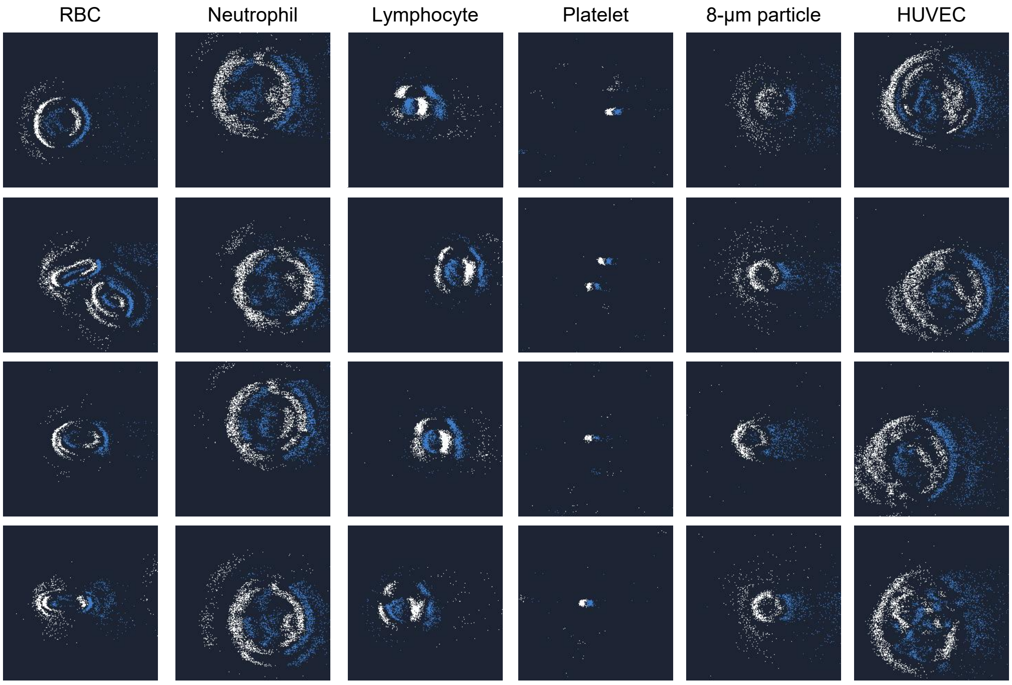

Number of activated pixels

	RBC	Neutrophil	Lymphocyte	Platelet	8-µm particle	HUVEC
Event data	1057	3279	1191	209	1231	2907
Frame data	50176					

Number of cell images per class

	RBC	Neutrophil	Lymphocyte	Platelet	8-µm particle	HUVEC
Original	2708	1087	2720	1859	4210	1246
Augmented	10832	4348	10880	7436	16840	4984

Figure 5.2 – Neuromorphic data curation for human blood cells (RBCs, neutrophils, lymphocytes, platelets), 8 μm particles, and HUVECs illustrated in Metavision Studio dark blue theme representation. The average number of activated pixels per cell type was calculated in event data and compared with frame data. The original number of sample cells and the number of sample cells after data augmentation were reported.

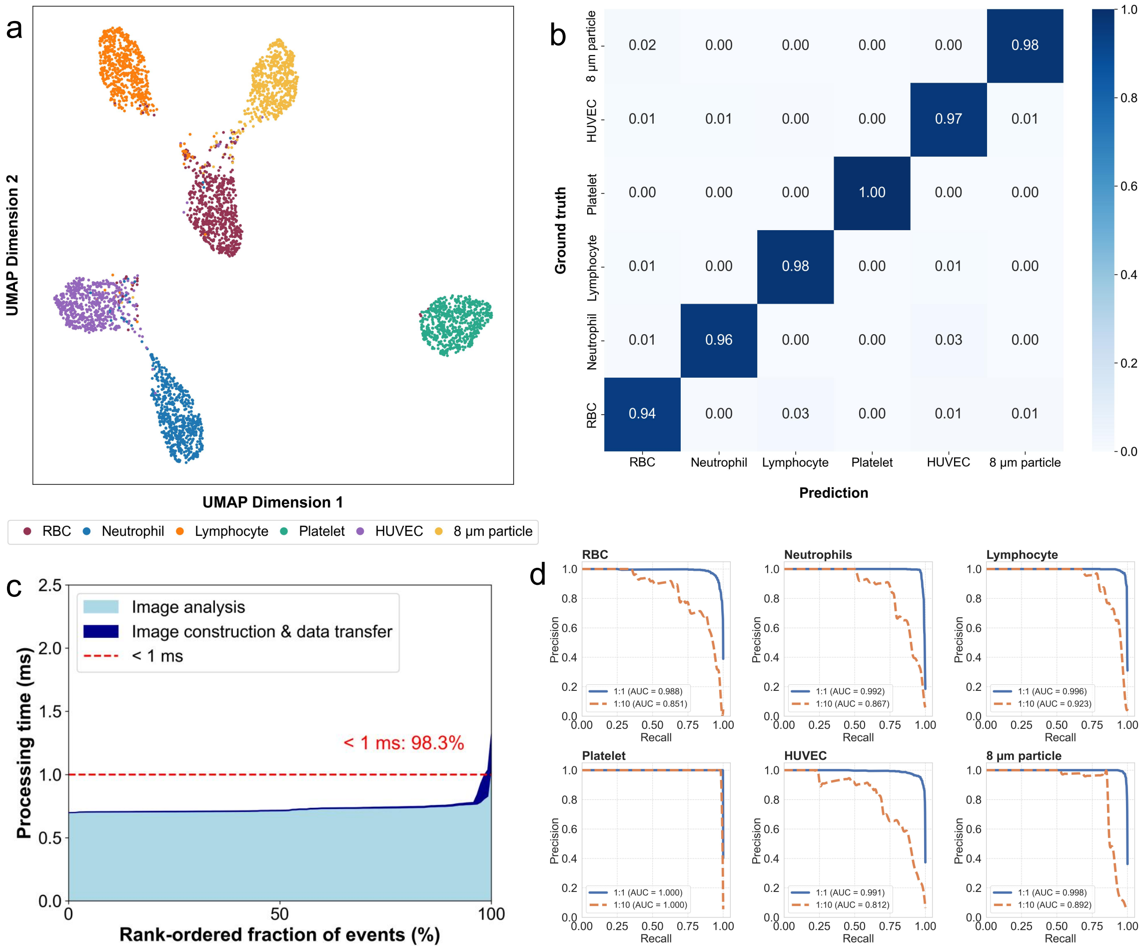

Figure 5.3 – CBAM-SNN-18 model performance based on neuromorphic cell data. **a** Cell clusters in UMAP revealing high-dimensional feature correlation in a 2D plot. **b** Confusion matrix based on each class's prediction outcome and ground truth annotation. **c** Processing time for image construction and data transfer with class inference time in a hierarchical arrangement of events from lowest to highest processing time. **d** Precision-recall curve for validation trained with 1:1 balanced and 1:10 imbalanced datasets.

5.2.3 Model performance

Cells with subtle morphological variation are critical to identify in a label-free state, as many cells can appear with similar physical traits in size and shape. Thus, the degree of feature NIC and DL can extract determines its applicability to conduct precise cell analysis and classification. In Fig. 5.3a, the learned features by the CBAM-SNN model were embedded into a UMAP for feature analysis, evaluating the high-dimensional feature extraction and correlation among classes. Most of the cell events were grouped into their respective clusters with a minor number of outliers resembling features across classes. Noticeably, the clusters of neutrophils and HUVECs were plotted relatively close together. This can be owing to the high resemblance of observable traits in size and internal complexity. RBCs and 8μm particles were also distributed similarly. A confusion matrix was constructed based on the network's prediction and ground truth in Fig. 5.3b. All predictive classes achieved a high ratio (>0.94) matching with the true annotation. The classification for platelets, lymphocytes, and 8μm particles accomplished outstanding scores of 1.00, 0.98, and 0.98. Given the fact that NIC can capture cells with subtle characteristic differences and these features can be recognised by DL models to accomplish outstanding performance in feature analysis and classification, NIC can be a suitable or advanced solution to address the conventional IFC challenges with its superior data efficiency, temporal resolution, and fluorescence sensitivity.

For ICS-like applications, the processing time from generating an image to decision-making is critical for overall throughput. A rank-ordered fraction of events based on processing time is shown in Fig. 5.3c with 98.3% events concluded within 1 ms. Compared to conventional feature gating, DL-based cell sorting was reported with an 11.5-fold increase in processing time but an 11-fold improvement in enrichment capability (Hayashi et al., 2023). In this study, we have achieved an average of 0.74 ms processing time compared with previously reported 4 to 5 ms measured on an image-by-image basis. Considering the continuous advancement in computing hardware and model architecture, the trade-off between speed and enrichment will be overcome or significantly alleviated in the future.

Furthermore, to accommodate the concentration variance among cells in the real biological environment, for example, human blood consists of 40–45% RBCs, 1% white blood cells, 1% platelets, or rare occurrences of endothelial cells in peripheral circulation (Samsel et al., 2013), a balanced and imbalanced dataset was introduced to the networks by maintaining a 1:1 ratio for targeted cells to total cells per class in the balanced case, and a 1:10 ratio in the imbalanced case. As shown in Fig. 5.3d, a precision-recall curve was plotted for each class's balanced and imbalanced conditions, with the Area Under the Curve (AUC) provided. The network exhibited a saturated curve with high precision and recall values in a 1:1 ratio, resulting in an average AUC of 0.994. Even the RBCs class, which had the lowest performance, achieved an AUC of 0.988, and the platelet class achieved a perfect score of 1.000. The model experienced a score drop with the imbalanced dataset but could still reach an average AUC of 0.891.

Traditional neural networks were designed to train with frame data, which requires cumbersome transformation to work with event streams. SNN has been proposed as a natural fit with NVS data to provide direct inference (Kugele et al., 2020; Vicente-Sola et al., 2025). To evaluate the compatibility of DL models with NIC, we trained two classic neural networks, ResNet-18 (He et al., 2016b) and EMS-ResNet-18 (Su et al., 2023), and developed a CBAM-SNN-18 model in Table 5.1 for comparison. While ResNet-18 achieved the highest performance, CBAM-SNN-18 reported comparable results with significantly lower computational requirements. This trade-off suggests that CBAM-SNN-18 may be better suited for lightweight, portable circumstances, whereas ResNet-18 is ideal for tasks prioritising maximum accuracy.

5.3 Method

5.3.1 Sample preparation

Human blood samples were collected into EDTA tubes from healthy volunteers following written informed consent under the Sydney Local Health District ethics protocol X23-0300. To ensure each footage contained the respective cells while maintaining a sufficient sample volume for data labelling and training purposes, the samples were treated with individual approaches to bulk separate the blood cells. Firstly, the platelet-containing plasma layer was separated following centrifugation at a speed of 800 g for 15 minutes. The plasma-depleted blood, layered with Ficoll-Paque (GE Healthcare, Sweden), underwent gradient centrifugation at a speed of 500 g, with no brake for 30 minutes to separate layers of different compositions in the blood. Lymphocytes were retrieved from the interface layer. At the bottom layer of the sample, RBCs were retrieved via conventional pipetting and diluted by a factor of 100 with PBS to reduce the excessive concentration of RBCs in the original sample. A second aliquot of the bottom layer was treated with red blood cell lysis to enrich the remaining neutrophils.

HUVECs (Lonza) were cultured in endothelial growth media (EGM-2, Lonza) at 37,° C and 5% CO_2. Cells were passaged using TrypLE Express (Gibco) and used between passage 4 and passage 6 for experiments. To prepare the cell suspension for microfluidic imaging experiments, dissociated HUVECs were resuspended in fresh warm media at a concentration of 6×10^5 cells/mL and used within 30 minutes.

5.3.2 Microfluidic imaging platform

A standard soft-lithography protocol (Zaouk et al., 2006) was used to fabricate a straight microfluidic channel (35 μm height, 100 μm width, and 30mm long) with PDMS (Sylgard® 184 Silicone Elastomer Kit, Dow Corning, UK). To ensure the sample cells travelled at a common depth for in-focus imaging, the channel was designed with a limited height to narrow the z-plane passage during delivery. An event camera, EVK4 (Prophesee, France), adopted in this experiment operated at 1280 × 720 resolution, 4.86×4.86 μm pixel size, with a time resolution equivalent to $> 10,000$ fps. The camera was integrated into an inverted microscope (IX73 Inverted Microscope, Olympus, Japan) to record the cell dynamics under 40 × magnification in phase contrast mode. The magnification was chosen to enhance the captured features and reveal the unique internal complexity of the cells. Metavision Studio software provided by Prophesee was utilised during the recording to optimise the visual feedback at an accumulation time of 200 μs.

For microfluidic delivery, the sample solution was loaded into a 1 mL syringe (Terumo Syringe, Terumo Corporation, Philippines) and actuated into the channel via a syringe pump (LEGATO 200 Syringe Pumps, KD Scientific Inc, USA) to induce a flow velocity of 4.78 mm/s. The flow velocity adopted in this experiment permitted sufficient exposure time to the sensor while maintaining a relatively fast speed. A new channel was implemented after each delivery class to avoid sample contamination from leftover particles.

5.3.3 Data preprocessing

As the cells were captured at a resolution of 1280 × 720, which is not ideal for single-cell analysis and machine learning import, the event data were first cropped into a 224 × 720 region of interest. A filtering technique that set an event threshold of 300 was applied to eliminate potential background noise and cell debris in the solution. Events were removed if the total event count fell below the threshold within the period. For platelets, a smaller threshold of 50 was adopted due to their significantly smaller size compared to the other samples.

The cell events were then cropped into 224 × 224 using K-means clustering to centre the samples within the images and data array. The event stream was divided into individual samples with a duration of 200 μs to generate 2D images for annotation and tensors with dimensions (x, y, p, t) for model training. Outliers with radical morphological differences, blurry edges, or out-of-focus images were manually discarded by the researcher, who had empirical experience working with NVS and targeted cell lines.

5.3.4 Model development

All training and validation were conducted on a Linux platform (Ubuntu 22.04) with an Intel i5-13600KF CPU and an NVIDIA RTX 2080 Ti GPU (22 GB VRAM). Event data can be cumbersome to process with traditional neural networks due to the unique event generation mechanism. SNNs are a natural match for implementation since they can be trained directly and exploit temporal information. They are also characterised by low latency, superior memory, and energy efficiency (Herbozo

Table 5.1 – CBAM-SNN-18, ResNet-18, and EMS-ResNet-18 performance comparison. The F1 score is weighted. Processing time is the sum of image preprocessing and inference time per sample. Inference memory represents the VRAM consumption of the model per sample.

	Accuracy (%)	**F1 Score** (%)	**Processing Time** (ms)	**Memory** (MB)	**Parameter** (M)	**Energy Consumption** (μJ)
CBAM-SNN-18	97.17	97.16	0.74	93.46	6.32	215
ResNet-18[a]	99.82	99.82	0.75	165.17	11.69	8417
EMS-Res-18[b]	96.21	96.18	0.70	88.77	6.32	170

[a] ResNet-18 and [b] EMS-ResNet utilised in this work adopted the original architecture in (He et al., 2016b) and (Su et al., 2023) trained on this dataset.

Contreras Sr et al., 2024). The forward propagation action in this network can be represented by Equ. 5.1 (Eshraghian et al., 2023b):

$$\begin{aligned} U_{i,j}^{t+1} &= \beta U_{i,j}^{t} + W_{i,j} X_{i,j}^{t+1} - R V_{thv} \\ S_{i,j}^{t+1} &= 1, if U_{i,j}^{t+1} \geq V_{thv} \end{aligned} \tag{5.1}$$

where $U_{i,j}^{t+1}$ and $U_{i,j}^{t}$ represented the membrane potential (V) in location (i,j),$W_{i,j}$ is the weight for different input spikes, S is the input spikes (V), β is the learnable parameter controlling membrane potential decay, R is the parameter represent the reset mechanism.

Surrogate Gradient was adopted to train our SNN directly. It replaced the infinite gradient with the arc-tan function in the backpropagation process to solve the dead neurons problem, which is shown in Equ. 5.2 (Eshraghian et al., 2023b; Fang et al., 2021; Neftci et al., 2019b).

$$\begin{aligned} S &\approx \frac{1}{\pi} \arctan \pi U \frac{\alpha}{2} \\ \frac{\partial S}{\partial U} &= \frac{1}{\pi} \frac{1}{(1 + (\pi U \frac{\alpha}{2})^2)} \end{aligned} \tag{5.2}$$

where S is the spikes this neuron produced (V), U is membrane potential (V), and α is a parameter with a default value of 2.

The model architecture of CBAM-SNN is demonstrated in Fig. 5.4a. As shown in Equ. 5.1, the LIF layer does not account for information from nearby neurons because

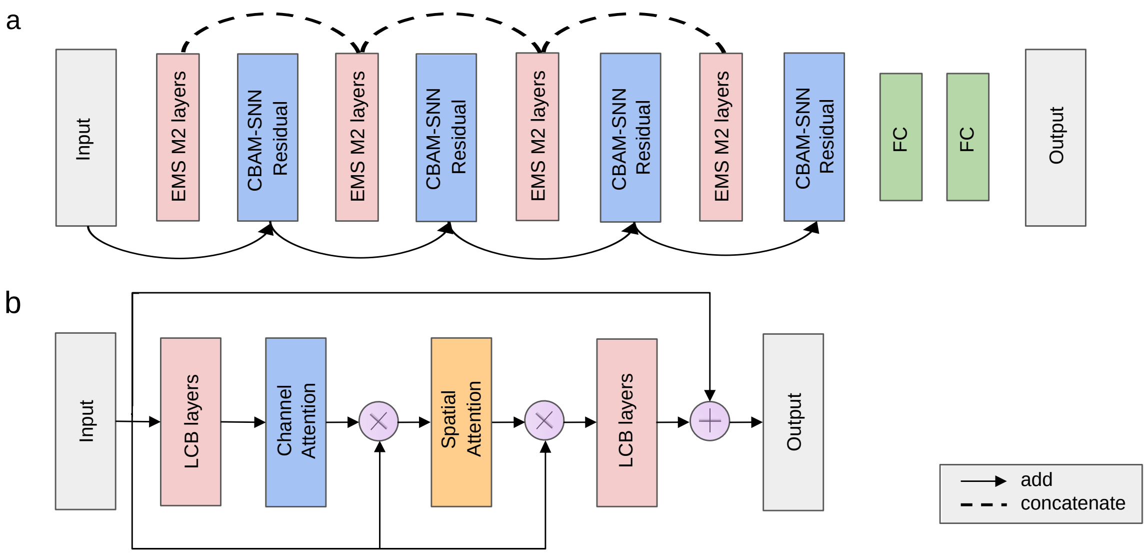

Figure 5.4 – CBAM-SNN model overall architecture. **a** The general structure of the CBAM-SNN model. Each basic block has three layers: one downsampling EMS block and two SNN-Residual blocks. Two bottleneck LCB layers construct the SNN-Residual block (He et al., 2016a). One local attention CBAM block is inserted into two LCB layers to build up the CBAM-SNN Residual layer. **b** The structure of the CBAM-SNN Residual block. When spikes enter this block, they first go through one LCB layer; channel-wise attention is calculated in Equ. 5.3 and multiplied with the input spikes. The result of this multiplication acts as the input of the spatial attention layer, repeats the previous operation, and then passes the result to the final LCB block.

its behaviour depends only on the history of its own signals. Therefore, the convolutional layers in a Convolutional Spiking Neural Networks (CSNN) are responsible for extracting spatial features. However, a few convolutional layers with small kernels in CSNN cannot sufficiently capture spatial features due to their limited receptive fields (Luo et al., 2016). Hence, to further enhance the network's capability without introducing excessive parameters and unnecessary computations, a local attention block, Convolutional Block Attention Module (CBAM), as shown in Fig. 5.4b, was implemented into the SNN-ResNet structure. This block is a widely known local attention mechanism that helps the network focus more on the important parts of the input data(Woo et al., 2018). It has already been used in many lightweight networks due to its efficiency (Chen et al., 2023; Wang et al., 2022; Zhang et al., 2024a). The combined local attention mechanism is expressed as Equ. 5.3,

$$\begin{aligned}\text{Attention}_C^t &= \text{Sigmoid}(\text{MLP}(\text{Avg}(X^t)) + \text{MLP}(\text{Max}(X^t)))\\ \text{Attention}_S^t &= \text{Sigmoid}(\text{Conv}(\text{Concat}(\text{Avg}(X^t), \text{Max}(X^t))))\end{aligned} \tag{5.3}$$

where t represents the current time step, X is the input spikes and $\text{MLP}(\cdot)$ is the shared multilayer perception, which has the same structure as SE-Block (Hu et al., 2018), $\text{Avg}(\cdot)$ is global average pooling, $\text{Max}(\cdot)$ is global Max pooling and $\text{Concat}(\cdot)$ represents the action concatenating two tensors in channel dimension.

All the blocks are built upon the fully spiked EMS block (Su et al., 2023), which consists of two branches. One branch consists of two consecutive LCB blocks constructed by LIF networks, batch normalisation layers, and convolution layers sequentially. The other branch is the residual branch, which consists of one Max-pooling layer used to transform the shape of the input data and avoid involving more Multiply-Accumulate (MAC) operations and one LCB block. In the second branch, the output from the two components is concatenated and acts as the result of the residual branch. The final output of this layer is the sum of these two branches, forming a fully spiked residual connection.

To avoid the possibility of under-fitting during training (Hu et al., 2024; Orhan and Pitkow, 2018), skip connections were added to all the local attention blocks, and residual connections were added to each down-sampling layer. These connections greatly enhance the performance of the model and render the training processes more stable (He et al., 2016a; Huang et al., 2017). To further reduce the MAC operation, all skip and residual connections use the same structure as EMS-ResNet used in EMS-Module 1 (Su et al., 2023), which consists of Max-pooling and LCB blocks. Moreover, depth-separable convolution layers were implemented to replace the normal convolution layers to reduce computation consumption (Chollet, 2017; Howard, 2017).

5.4 Conclusion

NVS has been widely adopted in the fields of auto-driving, aerial drone vision, and robotics, owing to its superior spatiotemporal resolution, data efficiency, low power consumption, and high dynamic range (Ayyad et al., 2023; Chen et al., 2020; Paredes-Vallés et al., 2024). However, this architecture has not yet been fully exploited in cell research, where it can be useful for handling large-scale cell data and time-critical applications. In this work, we presented the first neuromorphic cell dataset curated by NIC, including human blood cells, endothelial cells, and artificial microparticles, evaluating the event quality for representing the spatial content of biological structures. This dataset also serves as a baseline for healthy cell groups under NVS to compare with diseased cells for future diagnostic purposes. Our previous attempt confirmed a superior fluorescence sensitivity of NVS compared to traditional CMOS sensors (Zhang et al., 2023). Although the dataset curated is label-free, NIC can synergise with fluorescence signals for immunophenotyping and functional analysis. Additionally, the event-driven perception is not only an excellent candidate for IFC but also holds great potential for ICS, 3D cytometry, and other biological instrumentation requiring fast intervention or readout on samples.

To examine the feasibility of DL with NVS data for automating cell analysis and classification tasks, we developed a CBAM-SNN for evaluation. Cell feature analysis based on UMAP was illustrated, with all clusters distinctly separated. Cells with similar morphology were grouped in relatively close proximity but remained well-separated. These results highlight that NIC and DL are capable of capturing subtle features that distinguish different cell groups. The proposed networks also achieved promising performance across evaluation metrics, processing time, and imbalanced datasets. In the future, we will continue to expand this dataset by collecting additional cell lines or cell types specific to the biological context. The outcomes of this study demonstrate that NIC and DL form a powerful combination for AI-driven cell analysis and cytometry. By integrating efficient architectures in both imaging and processing methods, this approach has the potential to enable point-of-care solutions for research and diagnostic applications.

5.5 Ethic Statement

Human blood samples are obtained with full informed consent from healthy volunteers under the Sydney Local Health District ethics protocol X23-0300 in 2023. All procedures comply with institutional review board guidelines and respect participant privacy, confidentiality, and autonomy. Samples are used solely for research purposes, adhering to ethical guidelines for human biological materials.

5.6 Data Availability

All codes and data repositories are released under appropriate open-source licenses and are available via `https://github.com/NeuroSyd/CBAM-SNN`. Neuromorphic Cell Dataset can be accessed via `https://doi.org/10.6084/m9.figshare.27788970`.

5.7 Acknowledgement

S.W.C. acknowledges funding from The University of Sydney's Faculty of Engineering Scholarship.

5.8 Supplementary Information

Sample supplementary video footage of human blood cells is available via `https://doi.org/10.6084/m9.figshare.27789078`. Additional data curation and model development information can be viewed in supplementary content.

Chapter 6

Concluding Remarks

6.1 Thesis Contribution

In this dissertation, we included the complete development milestones of NIC distributed in each chapter. Our early investigation on developing this paradigm speculates the theoretical advantages of NVS over FBS for cytometry applications. It also provides the results of PS-particles under neuromorphic vision, evaluating the plausibility and quality of such sensing method in describing micro-scale targets with simplicity in shape. The effect of AT at different durations was also illustrated in this work for reference visual feedback and an indication of object dynamics. Most importantly, this research introduced the adoption of an event camera for cytometry applications for the first time, establishing a fundamental milestone for future research in this domain.

Although the implementation seems straightforward, significant effort is required to realise the functionalities and draw a conclusion about the idea. In the following research, we implemented the essential cytometric functions for cell counting and size estimation. Our performance was compared with a commercialised cytometer and yielded competitive results. The superior fluorescence sensitivity of NVS was also demonstrated in measuring FITC particles with low excitation power. This confirms the theoretical advantage of HDR (>120 dB) can suppress the performance of traditional FBSs in terms of fluorescence sensitivity. Considering many biomolecules exist in trace amounts, characterising these target cells or cellular components with fluorescence probes can result in compromised or missed information captured by FBS. Therefore, the advanced fluorescence sensitivity of NIC can deliver an enriched analysis on a broader range of cell types, proteins, enzymes and other biomolecules.

Moreover, we have investigated the compatibility of NIC with ML method to automate cell classification and detection. A SNN model, SNN-YOLO was developed to detect particles with similar morphology, including PS-particles with different sizes, THP-1 and LL/2 cells. The proposed network has achieved a 97.4% accuracy in cell detection, outperforming the baseline model, YOLOv3 that was trained on frame data, by 1.2%. This outcome also confirmed the validity of integrating the entire framework based on neuromorphic architecture for data-efficient and possibly miniaturised cytometric devices.

Recently, the NIC platform has been developed in varied modalities and ML approaches. Despite these advancements, the majority of the work is performed only with artificial particles or limited biological samples without capturing complexity in structure. To examine the imaging capacity of the platform and train the algorit hm to learn more diverse morphology, our following work curated the first neuromorphic cell dataset including RBCs, neutrophils, lymphocytes, platelets, HUVECs and other micro-scale targets with well-defined structure. This dataset can serve as a baseline for healthy cell groups under NVS to compare with diseased cells for future diagnostic purposes. Our hybrid model, CBAM-SNN has yielded a high score of 97% accuracy and F1 score with a significant reduction in computational resources compared to other networks. The extracted features by CBAM-SNN were embedded into UMAP for feature analysis, evaluating the high-dimensional feature extraction and correlation among classes. This work proved that the current lightweight ML architecture is able to distinguish and provide analysis on clinical-significant cells with subtle differences under neuromorphic vision.

6.2 Future Research Directions

Although our NIC platform has advanced with numerous functionalities, it has not yet reached the full capabilities of a commercialised cytometer. Future endeavours should include the integration of additional features and the compacting of the system into a more portable, ready-to-use platform. One major drawback of the current system is the cumbersome calibration work on focusing the sample cells. As in a flow system, objects can pass through the field of view in an extremely brief window and normally, focusing on a static sample is a straightforward solution. However, with NVS a dynamic scene must be maintained to allow the firing of the pixel for visualisation. Calibration, while samples are in motion or vibration on the platform, is currently a primitive solution. An autofocus technique is critical to provide efficiency in the workflow and reach the sharpest event representation. Moreover, a customised NVS or paired with specialised techniques for cytometry application can further enhance the capacity of the platform to achieve higher throughput and resolution. For example, CCD sensor coupled with a time delay integration technique has been adopted to increase the sensitivity to detect weak fluorescence signals and avoid motion blur(Basiji et al., 2007; Elliott, 2009; Han et al., 2016). Multiple fields of view onto CMOS camera also burst the throughput by magnitudes and circumvent the trade-off (Schonbrun et al., 2012). Similar strategies can be implemented with NVS to elevate the imaging performance. Considering the superior data efficiency, sensitivity and temporal resolution of NVS, this paradigm should be also encouraged on ICS, 3D cytometry and other biological instrumentation requiring fast intervention or readout on samples.

In the aspect of ML, our latest model, CBAM-SNN is capable of classifying and providing analysis on human blood cells and cells with subtle differences. The AUC score was dropped when the imbalance dataset was introduced. This can indicate that the model is not robust enough to handle a largely imbalanced sample size, where in nature, biological samples can composite with cells in extremely different concentrations. Additionally, a cytometer screens a significantly diverse range of cell types for multi-parametric analysis. To implement AI in cytometry applications, the network must be able to identify these cells with high confidence. In the future, we will continue to build on this dataset by including broader cell classes or cell types that are specific to their biological context. Moreover, the network was operated on a conventional GPU, applying the entire computation process on neuromorphic hardware could significantly enhance processing speed, thereby mitigating the trade-off.

This project was developed from scratch without any preceding research on the topic to a functional platform and feasibility study that can classify cells with complicated structures. Although the current platform has not yet equipped with full capabilities for a commercialised cytometer, we believe that the continuous efforts and development of NIC can enable an AI, high-throughput and sensitive cell-analytic tool for point-of-care clinical and research solutions.

List of References

Abreu, S., Gouda, M., Lugnan, A., and Bienstman, P. (2023). Flow cytometry with event-based vision and spiking neuromorphic hardware. In *Proceedings of the IEEE/CVF Conference on Computer Vision and Pattern Recognition*, pages 4138–4146.

Adan, A., Alizada, G., Kiraz, Y., Baran, Y., and Nalbant, A. (2017). Flow cytometry: basic principles and applications. *Critical reviews in biotechnology*, 37(2):163–176.

Alsalem, M., Zaidan, A., Zaidan, B., Hashim, M., Madhloom, H., Azeez, N., and Alsyisuf, S. (2018). A review of the automated detection and classification of acute leukaemia: Coherent taxonomy, datasets, validation and performance measurements, motivation, open challenges and recommendations. *Computer methods and programs in biomedicine*, 158:93–112.

Alzubaidi, L., Fadhel, M. A., Al-Shamma, O., Zhang, J., and Duan, Y. (2020). Deep learning models for classification of red blood cells in microscopy images to aid in sickle cell anemia diagnosis. *Electronics*, 9(3):427.

Aragona, M., Panciera, T., Manfrin, A., Giulitti, S., Michielin, F., Elvassore, N., Dupont, S., and Piccolo, S. (2013). A mechanical checkpoint controls multicellular growth through yap/taz regulation by actin-processing factors. *Cell*, 154(5):1047–1059.

Arvaniti, E. and Claassen, M. (2017). Sensitive detection of rare disease-associated cell subsets via representation learning. *Nature Communications*, 8(1).

Ayyad, A., Halwani, M., Swart, D., Muthusamy, R., Almaskari, F., and Zweiri, Y. (2023). Neuromorphic vision based control for the precise positioning of robotic drilling systems. *Robotics and Computer-Integrated Manufacturing*, 79:102419.

Barteneva, N. S., Fasler-Kan, E., and Vorobjev, I. A. (2012). Imaging flow cytometry: Coping with heterogeneity in biological systems. *Journal of Histochemistry & Cytochemistry*, 60(10):723–733.

Basiji, D. A., Ortyn, W. E., Liang, L., Venkatachalam, V., and Morrissey, P. (2007). Cellular image analysis and imaging by flow cytometry. *Clinics in laboratory medicine*, 27(3):653–670.

Benosman, R., Ieng, S.-H., Clercq, C., Bartolozzi, C., and Srinivasan, M. (2012). Asynchronous frameless event-based optical flow. *Neural Networks*, 27:32–37.

Blann, A. D., Woywodt, A., Bertolini, F., Bull, T. M., Buyon, J. P., Clancy, R. M., Haubitz, M., Hebbel, R. P., Lip, G. Y., Mancuso, P., et al. (2005). Circulating endothelial cells. *Thrombosis and haemostasis*, 93(02):228–235.

Boldú, L., Merino, A., Acevedo, A., Molina, A., and Rodellar, J. (2021). A deep learning model (alnet) for the diagnosis of acute leukaemia lineage using peripheral blood cell images. *Computer Methods and Programs in Biomedicine*, 202:105999.

Boutros, M., Heigwer, F., and Laufer, C. (2015). Microscopy-based high-content screening. *Cell*, 163(6):1314–1325.

Buchser, W., Collins, M., Garyantes, T., Guha, R., Haney, S., Lemmon, V., Li, Z., and Trask, O. J. (2014). Assay development guidelines for image-based high content screening, high content analysis and high content imaging. *Assay guidance manual [Internet]*.

Buggenthin, F., Buettner, F., Hoppe, P. S., Endele, M., Kroiss, M., Strasser, M., Schwarzfischer, M., Loeffler, D., Kokkaliaris, K. D., Hilsenbeck, O., et al. (2017). Prospective identification of hematopoietic lineage choice by deep learning. *Nature methods*, 14(4):403–406.

Cai, L., Dalal, C. K., and Elowitz, M. B. (2008). Frequency-modulated nuclear localization bursts coordinate gene regulation. *Nature*, 455(7212):485–490.

Caicedo, J. C., Cooper, S., Heigwer, F., Warchal, S., Qiu, P., Molnar, C., Vasilevich, A. S., Barry, J. D., Bansal, H. S., Kraus, O., et al. (2017). Data-analysis strategies for image-based cell profiling. *Nature methods*, 14(9):849–863.

Chen, A. Y., Yu, C., Gatto, B., and LIu, L. F. (1993). Dna minor groove-binding ligands: a different class of mammalian dna topoisomerase i inhibitors. *Proceedings of the National Academy of Sciences*, 90(17):8131–8135.

Chen, C. S., Mrksich, M., Huang, S., Whitesides, G. M., and Ingber, D. E. (1997). Geometric control of cell life and death. *Science*, 276(5317):1425–1428.

Chen, G., Cao, H., Conradt, J., Tang, H., Rohrbein, F., and Knoll, A. (2020). Event-based neuromorphic vision for autonomous driving: A paradigm shift for bio-inspired visual sensing and perception. *IEEE Signal Processing Magazine*, 37(4):34–49.

Chen, L., Yao, H., Fu, J., and Ng, C. T. (2023). The classification and localization of crack using lightweight convolutional neural network with cbam. *Engineering Structures*, 275:115291.

Cheng, L., Karkhanis, P., Gokbag, B., Liu, Y., and Li, L. (2022). Dgcytof: Deep learning with graphic cluster visualization to predict cell types of single cell mass cytometry data. *PLOS Computational Biology*, 18(4).

Chollet, F. (2017). Xception: Deep learning with depthwise separable convolutions. In *Proceedings of the IEEE Conference on Computer Vision and Pattern Recognition (CVPR)*, pages 1251–1258.

Cossarizza, A., Chang, H.-D., Radbruch, A., Acs, A., Adam, D., Adam-Klages, S., Agace, W. W., Aghaeepour, N., Akdis, M., Allez, M., et al. (2019). Guidelines for the use of flow cytometry and cell sorting in immunological studies. *European journal of immunology*, 49(10):1457–1973.

De Wit, G., Danial, J. S., Kukura, P., and Wallace, M. I. (2015). Dynamic label-free imaging of lipid nanodomains. *Proceedings of the National Academy of Sciences*, 112(40):12299–12303.

Di Carlo, D. (2009). Inertial microfluidics. *Lab on a Chip*, 9(21):3038.

Drescher, H., Weiskirchen, S., and Weiskirchen, R. (2021). Flow cytometry: A blessing and a curse. *Biomedicines*, 9(11):1613.

Elliott, G. S. (2009). Moving pictures: imaging flow cytometry for drug development. *Combinatorial chemistry & high throughput screening*, 12(9):849–859.

Eshraghian, J. K. and Lu, W. D. (2022). The fine line between dead neurons and sparsity in binarized spiking neural networks. *arXiv preprint arXiv:2201.11915*.

Eshraghian, J. K., Ward, M., Neftci, E., Wang, X., Lenz, G., Dwivedi, G., Bennamoun, M., Jeong, D. S., and Lu, W. D. (2023a). Training spiking neural networks using lessons from deep learning. *Proceedings of the IEEE*, 111(9):1016–1054.

Eshraghian, J. K., Ward, M., Neftci, E. O., Wang, X., Lenz, G., Dwivedi, G., Bennamoun, M., Jeong, D. S., and Lu, W. D. (2023b). Training spiking neural networks using lessons from deep learning. *Proceedings of the IEEE*, 111(9):1016–1054.

Eulenberg, P., Köhler, N., Blasi, T., Filby, A., Carpenter, A. E., Rees, P., Theis, F. J., and Wolf, F. A. (2017). Reconstructing cell cycle and disease progression using deep learning. *Nature Communcations*, 8(1):463.

Fang, W., Yu, Z., Chen, Y., Masquelier, T., Huang, T., and Tian, Y. (2021). Incorporating learnable membrane time constant to enhance learning of spiking neural networks.

Farhadi, A. and Redmon, J. (2018). YOLOv3: An incremental improvement.

Freudiger, C. W., Min, W., Saar, B. G., Lu, S., Holtom, G. R., He, C., Tsai, J. C., Kang, J. X., and Xie, X. S. (2008). Label-free biomedical imaging with high sensitivity by stimulated raman scattering microscopy. *Science*, 322(5909):1857–1861.

Gallego, G., Delbrück, T., Orchard, G., Bartolozzi, C., Taba, B., Censi, A., Leutenegger, S., Davison, A. J., Conradt, J., Daniilidis, K., et al. (2020). Event-based vision: A survey. *IEEE Transactions on Pattern Analysis and Machine Intelligence*, 44(1):154–180.

Gorecki, A. M., Anyaegbu, C. C., Fitzgerald, M., Fuller, K. A., and Anderton, R. S. (2025). Imaging flow cytometry reveals lps-induced changes to intracellular intensity and distribution of α-synuclein in a tlr4-dependent manner in stc-1 cells. *Methods*, 234:93–111.

Görner, W., Durchschlag, E., Martinez-Pastor, M. T., Estruch, F., Ammerer, G., Hamilton, B., Ruis, H., and Schüller, C. (1998). Nuclear localization of the c2h2 zinc finger protein msn2p is regulated by stress and protein kinase a activity. *Genes & development*, 12(4):586–597.

Gouda, M., Abreu, S., and Bienstman, P. (2024a). Clustering and classification of fungal cells and pmma microparticles: Unsupervised and supervised learning using k-means, pca, logistic regression and spiking neural networks on event-based cytometry datasets. In *2024 24th International Conference on Transparent Optical Networks (ICTON)*, pages 1–4. IEEE.

Gouda, M., Abreu, S., and Bienstman, P. (2024b). Surrogate gradient learning in spiking networks trained on event-based cytometry dataset. *Optics Express*, 32(9):16260–16272.

Grimwade, L. F., Fuller, K. A., and Erber, W. N. (2017). Applications of imaging flow cytometry in the diagnostic assessment of acute leukaemia. *Methods*, 112:39–45.

Han, Y., Gu, Y., Zhang, A. C., and Lo, Y.-H. (2016). Imaging technologies for flow cytometry. *Lab on a Chip*, 16(24):4639–4647.

Hao, N., Budnik, B. A., Gunawardena, J., and O'Shea, E. K. (2013). Tunable signal processing through modular control of transcription factor translocation. *Science*, 339(6118):460–464.

Hayashi, M., Ohnuki, S., Tsai, Y., Kondo, N., Zhou, Y., Zhang, H., Ishii, N. T., Ding, T., Herbig, M., Isozaki, A., et al. (2023). Is AI essential? Examining the need for deep learning in image-activated sorting of saccharomyces cerevisiae. *Lab on a Chip*, 23(19):4232–4244.

He, K., Zhang, X., Ren, S., and Sun, J. (2016a). Deep residual learning for image recognition. In *IEEE Conference on Computer Vision and Pattern Recognition (CVPR)*, pages 770–778.

He, K., Zhang, X., Ren, S., and Sun, J. (2016b). Deep residual learning for image recognition. In *IEEE Conference on Computer Vision and Pattern Recognition (CVPR)*, pages 770–778.

He, W., Feng, Y., Zhu, J., Chai, H., and Wang, W. (2022). Neuromorphic-enabled event-based deep imaging flow cytometry. In *26th International Conference on Miniaturized Systems for Chemistry and Life Sciences*, volume 10, page 2.

He, W., Zhu, J., Feng, Y., Liang, F., You, K., Chai, H., Sui, Z., Hao, H., Li, G., Zhao, J., et al. (2024). Neuromorphic-enabled video-activated cell sorting. *Nature Communications*, 15(1):10792.

Herbozo Contreras Sr, L. F., Yu Sr, L., Huang Sr, Z., Zhang Sr, Z., Nikpour Sr, A., and Kavehei Sr, O. (2024). Tiny dlif: A dendritic spiking neural network enabling a time-domain energy-efficient seizure detection system. *medRxiv*, pages 2024–05.

Hirano, M., Ando, R., Shimozono, S., Sugiyama, M., Takeda, N., Kurokawa, H., Deguchi, R., Endo, K., Haga, K., Takai-Todaka, R., et al. (2022). A highly photostable and bright green fluorescent protein. *Nature biotechnology*, 40(7):1132–1142.

Hoebe, R., Van Oven, C., Gadella Jr, T., Dhonukshe, P., Van Noorden, C., and Manders, E. (2007). Controlled light-exposure microscopy reduces photobleaching and phototoxicity in fluorescence live-cell imaging. *Nature biotechnology*, 25(2):249–253.

Holzner, G., Mateescu, B., van Leeuwen, D., Cereghetti, G., Dechant, R., Stavrakis, S., and deMello, A. (2021). High-throughput multiparametric imaging flow cytometry: toward diffraction-limited sub-cellular detection and monitoring of sub-cellular processes. *Cell Reports*, 34(10).

Howard, A. G. (2017). MobileNets: Efficient convolutional neural networks for mobile vision applications. *arXiv preprint arXiv:1704.04861*.

Howell, J., Hammarton, T. C., Altmann, Y., and Jimenez, M. (2020). High-speed particle detection and tracking in microfluidic devices using event-based sensing. *Lab on a Chip*, 20(16):3024–3035.

Hu, J., Shen, L., and Sun, G. (2018). Squeeze-and-excitation networks. In *IEEE/CVF Conference on Computer Vision and Pattern Recognition*, pages 7132–7141.

Hu, Y., Deng, L., Wu, Y., Yao, M., and Li, G. (2024). Advancing spiking neural networks toward deep residual learning. *IEEE Transactions on Neural Networks and Learning Systems*, pages 1–15.

Hu, Z., Bhattacharya, S., and Butte, A. J. (2022). Application of machine learning for cytometry data. *Frontiers in Immunology*, 12.

Hu, Z., Tang, A., Singh, J., Bhattacharya, S., and Butte, A. J. (2020). A robust and interpretable end-to-end deep learning model for cytometry data. *Proceedings of the National Academy of Sciences*, 117(35):21373–21380.

Huang, G., Liu, Z., Van Der Maaten, L., and Weinberger, K. Q. (2017). Densely connected convolutional networks. In *IEEE Conference on Computer Vision and Pattern Recognition (CVPR)*, pages 2261–2269.

Huang, K., Matsumura, H., Zhao, Y., Herbig, M., Yuan, D., Mineharu, Y., Harmon, J., Findinier, J., Yamagishi, M., Ohnuki, S., et al. (2022). Deep imaging flow cytometry. *Lab on a Chip*, 22(5):876–889.

Icha, J., Weber, M., Waters, J. C., and Norden, C. (2017). Phototoxicity in live fluorescence microscopy, and how to avoid it. *BioEssays*, 39(8):1700003.

Isozaki, A., Mikami, H., Tezuka, H., Matsumura, H., Huang, K., Akamine, M., Hiramatsu, K., Iino, T., Ito, T., Karakawa, H., et al. (2020a). Intelligent image-activated cell sorting 2.0. *Lab on a Chip*, 20(13):2263–2273.

Isozaki, A., Nakagawa, Y., Loo, M., Shibata, Y., Tanaka, N., Setyaningrum, D., Park, J.-W., Shirasaki, Y., Mikami, H., Huang, D., et al. (2020b). Sequentially addressable dielectrophoretic array for high-throughput sorting of large-volume biological compartments. *Science advances*, 6(22):eaba6712.

Izumi, S., Urano, Y., Hanaoka, K., Terai, T., and Nagano, T. (2009). A simple and effective strategy to increase the sensitivity of fluorescence probes in living cells. *Journal of the American Chemical Society*, 131(29):10189–10200.

Joshi, S. and Yu, D. (2017). Immunofluorescence. In *Basic science methods for clinical researchers*, pages 135–150. Elsevier.

Khan, S. S., Solomon, M. A., and McCoy Jr, J. P. (2005). Detection of circulating endothelial cells and endothelial progenitor cells by flow cytometry. *Cytometry Part B: Clinical Cytometry: The Journal of the International Society for Analytical Cytology*, 64(1):1–8.

Kilian, K. A., Bugarija, B., Lahn, B. T., and Mrksich, M. (2010). Geometric cues for directing the differentiation of mesenchymal stem cells. *Proceedings of the National Academy of Sciences*, 107(11):4872–4877.

Kim, S., Park, S., Na, B., and Yoon, S. (2020). Spiking-yolo: Spiking neural network for energy-efficient object detection. *Proceedings of the AAAI Conference on Artificial Intelligence*, 34(07):11270–11277.

Kim, Y. and Panda, P. (2021). Revisiting batch normalization for training low-latency deep spiking neural networks from scratch. *Frontiers in Neuroscience*, 15.

Kugele, A., Pfeil, T., Pfeiffer, M., and Chicca, E. (2020). Efficient processing of spatio-temporal data streams with spiking neural networks. *Frontiers in neuroscience*, 14:512192.

LaBelle, C. A., Massaro, A., Cortés-Llanos, B., Sims, C. E., and Allbritton, N. L. (2021). Image-based live cell sorting. *Trends in biotechnology*, 39(6):613–623.

Laissue, P. P., Alghamdi, R. A., Tomancak, P., Reynaud, E. G., and Shroff, H. (2017). Assessing phototoxicity in live fluorescence imaging. *Nature methods*, 14(7):657–661.

Lapicque, L. (1907). Recherches quantitatives sur l'excitation electrique des nerfs. *J. Physiol. Paris*, 9:620–635.

Lee, K., Kim, S.-E., Doh, J., Kim, K., and Chung, W. K. (2021). User-friendly image-activated microfluidic cell sorting technique using an optimized, fast deep learning algorithm. *Lab on a Chip*, 21(9):1798–1810.

Li, X., Li, Y., Zhou, Y., Wu, J., Zhao, Z., Fan, J., Deng, F., Wu, Z., Xiao, G., He, J., et al. (2023). Real-time denoising enables high-sensitivity fluorescence time-lapse imaging beyond the shot-noise limit. *Nature Biotechnology*, 41(2):282–292.

Li, Y., Nowak, C. M., Pham, U., Nguyen, K., and Bleris, L. (2021). Cell morphology-based machine learning models for human cell state classification. *NPJ Systems Biology and Applications*, 7(1):23.

Lichtsteiner, P., Posch, C., and Delbruck, T. (2008). A 128×128 120 dB 15μs latency asynchronous temporal contrast vision sensor. *IEEE Journal of Solid-State Circuits*, 43(2):566–576.

Lippeveld, M., Knill, C., Ladlow, E., Fuller, A., Michaelis, L. J., Saeys, Y., Filby, A., and Peralta, D. (2019). Classification of human white blood cells using machine learning for stain-free imaging flow cytometry. *Cytometry Part A*, 97(3):308–319.

Loshchilov, I. and Hutter, F. (2019). Decoupled weight decay regularization.

Luo, W., Li, Y., Urtasun, R., and Zemel, R. (2016). Understanding the effective receptive field in deep convolutional neural networks. *Advances in Neural Information Processing Systems*, 29.

Mackinder, L. C., Chen, C., Leib, R. D., Patena, W., Blum, S. R., Rodman, M., Ramundo, S., Adams, C. M., and Jonikas, M. C. (2017). A spatial interactome reveals the protein organization of the algal co2-concentrating mechanism. *Cell*, 171(1):133–147.

McKinnon, K. M. (2018). Flow cytometry: An overview. *Current Protocols in Immunology*, 120(1):5–1.

Merola, F., Memmolo, P., Miccio, L., Savoia, R., Mugnano, M., Fontana, A., D'ippolito, G., Sardo, A., Iolascon, A., Gambale, A., et al. (2017). Tomographic flow cytometry by digital holography. *Light: Science & Applications*, 6(4):e16241–e16241.

Mertz, J. (2011). Optical sectioning microscopy with planar or structured illumination. *Nature methods*, 8(10):811–819.

Miltenburger, H., Sachse, G., and Schliermann, M. (1987). S-phase cell detection with a monoclonal antibody. *Developments in Biological Standardization*, 66:91–99.

Moor, A. E., Golan, M., Massasa, E. E., Lemze, D., Weizman, T., Shenhav, R., Baydatch, S., Mizrahi, O., Winkler, R., Golani, O., et al. (2017). Global mrna polarization regulates translation efficiency in the intestinal epithelium. *Science*, 357(6357):1299–1303.

Morais, P., Nelles, D., Vij, V., Al-Kassou, B., Weber, M., Nickenig, G., Schrickel, J. W., Vilaca, J. L., and Sedaghat, A. (2022). Assessment of laa strain and thrombus mobility and its impact on thrombus resolution—added-value of a novel echocardiographic thrombus tracking method. *Cardiovascular Engineering and Technology*, 13(6):950–960.

Mueggler, E., Rebecq, H., Gallego, G., Delbruck, T., and Scaramuzza, D. (2017). The event-camera dataset and simulator: Event-based data for pose estimation, visual odometry, and slam. *The International Journal of Robotics Research*, 36(2):142–149.

Nagai, T., Yamada, S., Tominaga, T., Ichikawa, M., and Miyawaki, A. (2004). Expanded dynamic range of fluorescent indicators for ca2+ by circularly permuted yellow fluorescent proteins. *Proceedings of the National Academy of Sciences*, 101(29):10554–10559.

Nawaz, A. A., Soteriou, D., Xu, C. K., Goswami, R., Herbig, M., Guck, J., and Girardo, S. (2023). Image-based cell sorting using focused travelling surface acoustic waves. *Lab on a Chip*, 23:372–387.

Nawaz, A. A., Urbanska, M., Herbig, M., Nötzel, M., Kräter, M., Rosendahl, P., Herold, C., Toepfner, N., Kubánková, M., Goswami, R., et al. (2020). Intelligent image-based deformation-assisted cell sorting with molecular specificity. *Nature Methods*, 17(6):595–599.

Neftci, E. O., Mostafa, H., and Zenke, F. (2019a). Surrogate gradient learning in spiking neural networks: Bringing the power of gradient-based optimization to spiking neural networks. *IEEE Signal Processing Magazine*, 36(6):51–63.

Neftci, E. O., Mostafa, H., and Zenke, F. (2019b). Surrogate gradient learning in spiking neural networks: Bringing the power of gradient-based optimization to spiking neural networks. *IEEE Signal Processing Magazine*, 36(6):51–63.

Nitta, N., Sugimura, T., Isozaki, A., Mikami, H., Hiraki, K., Sakuma, S., Iino, T., Arai, F., Endo, T., Fujiwaki, Y., et al. (2018). Intelligent image-activated cell sorting. *Cell*, 175(1):266–276.

Orhan, E. and Pitkow, X. (2018). Skip connections eliminate singularities. In *International Conference on Learning Representations*.

Pan, L., Hartley, R., Scheerlinck, C., Liu, M., Yu, X., and Dai, Y. (2020). High frame rate video reconstruction based on an event camera. *IEEE Transactions on Pattern Analysis and Machine Intelligence*, 44(5):2519–2533.

Paredes-Vallés, F., Hagenaars, J. J., Dupeyroux, J., Stroobants, S., Xu, Y., and de Croon, G. (2024). Fully neuromorphic vision and control for autonomous drone flight. *Science Robotics*, 9(90):eadi0591.

Pereira, V. M., Bonnefous, O., Ouared, R., Brina, O., Stawiaski, J., Aerts, H., Ruijters, D., Narata, A., Bijlenga, P., Schaller, K., et al. (2013). A dsa-based method using contrast-motion estimation for the assessment of the intra-aneurysmal flow changes induced by flow-diverter stents. *American Journal of Neuroradiology*, 34(4):808–815.

Pernas, L., Bean, C., Boothroyd, J. C., and Scorrano, L. (2018). Mitochondria restrict growth of the intracellular parasite toxoplasma gondii by limiting its uptake of fatty acids. *Cell metabolism*, 27(4):886–897.

Podgorski, K. and Ranganathan, G. (2016). Brain heating induced by near-infrared lasers during multiphoton microscopy. *Journal of neurophysiology*, 116(3):1012–1023.

Qiu, P., Simonds, E. F., Bendall, S. C., Gibbs, K. D., Bruggner, R. V., Linderman, M. D., Sachs, K., Nolan, G. P., and Plevritis, S. K. (2011). Extracting a cellular hierarchy from high-dimensional cytometry data with spade. *Nature Biotechnology*, 29(10):886–891.

Rane, A. S., Rutkauskaite, J., deMello, A., and Stavrakis, S. (2017). High-throughput multi-parametric imaging flow cytometry. *Chem*, 3(4):588–602.

Rees, P., Summers, H. D., Filby, A., Carpenter, A. E., and Doan, M. (2022). Imaging flow cytometry. *Nature Reviews Methods Primers*, 2(1):86.

Reggeti, F. and Bienzle, D. (2011). Flow cytometry in veterinary oncology. *Veterinary pathology*, 48(1):223–235.

Rožanc, J., Finšgar, M., and Maver, U. (2021). Progressive use of multispectral imaging flow cytometry in various research areas. *Analyst*, 146(16):4985–5007.

Saeys, Y., Van Gassen, S., and Lambrecht, B. N. (2016). Computational flow cytometry: helping to make sense of high-dimensional immunology data. *Nature Reviews Immunology*, 16(7):449–462.

Salek, M., Li, N., Chou, H.-P., Saini, K., Jovic, A., Jacobs, K. B., Johnson, C., Lu, V., Lee, E. J., Chang, C., et al. (2023). COSMOS: a platform for real-time morphology-based, label-free cell sorting using deep learning. *Communications Biology*, 6(1):971.

Salto-Tellez, M. (2018). More than a decade of molecular diagnostic cytopathology leading diagnostic and therapeutic decision-making. *Archives of pathology & laboratory medicine*, 142(4):443–445.

Samsel, L., Dagur, P. K., Raghavachari, N., Seamon, C., Kato, G. J., and McCoy Jr, J. P. (2013). Imaging flow cytometry for morphologic and phenotypic characterization of rare circulating endothelial cells. *Cytometry Part B: Clinical Cytometry*, 84(6):379–389.

Sant, M., Allemani, C., Tereanu, C., De Angelis, R., Capocaccia, R., Visser, O., Marcos-Gragera, R., Maynadié, M., Simonetti, A., Lutz, J.-M., et al. (2010). Incidence of hematologic malignancies in europe by morphologic subtype: results of the haemacare project. *Blood, The Journal of the American Society of Hematology*, 116(19):3724–3734.

Schmidhuber, J., Hochreiter, S., et al. (1997). Long short-term memory. *Neural Comput*, 9(8):1735–1780.

Schonbrun, E., Gorthi, S. S., and Schaak, D. (2012). Microfabricated multiple field of view imaging flow cytometry. *Lab on a Chip*, 12(2):268–273.

Schraivogel, D., Kuhn, T. M., Rauscher, B., Rodríguez-Martínez, M., Paulsen, M., Owsley, K., Middlebrook, A., Tischer, C., Ramasz, B., Ordoñez-Rueda, D., et al. (2022). High-speed fluorescence image–enabled cell sorting. *Science*, 375(6578):315–320.

Sciambi, A. and Abate, A. R. (2015). Accurate microfluidic sorting of droplets at 30 khz. *Lab on a Chip*, 15(1):47–51.

Sen, B., Ganesh, A., Bhan, A., Dixit, S., and Goyal, A. (2021). Machine learning based diagnosis and classification of sickle cell anemia in human rbc. In *2021 Third International Conference on Intelligent Communication Technologies and Virtual Mobile Networks (ICICV)*, pages 753–758. IEEE.

Sesen, M. and Whyte, G. (2020). Image-based single cell sorting automation in droplet microfluidics. *Scientific reports*, 10(1):8736.

Shapiro, H. M. and Telford, W. G. (2009). Lasers for flow cytometry. *Current protocols in cytometry*, 49(1):1–9.

Shields Iv, C. W., Reyes, C. D., and López, G. P. (2015). Microfluidic cell sorting: a review of the advances in the separation of cells from debulking to rare cell isolation. *Lab on a Chip*, 15(5):1230–1249.

Skylaki, S., Hilsenbeck, O., and Schroeder, T. (2016). Challenges in long-term imaging and quantification of single-cell dynamics. *Nature Biotechnology*, 34(11):1137–1144.

Stirling, D. R., Swain-Bowden, M. J., Lucas, A. M., Carpenter, A. E., Cimini, B. A., and Goodman, A. (2021). Cellprofiler 4: improvements in speed, utility and usability. *BMC bioinformatics*, 22:1–11.

Su, Q., Chou, Y., Hu, Y., Li, J., Mei, S., Zhang, Z., and Li, G. (2023). Deep directly-trained spiking neural networks for object detection. *2023 IEEE/CVF International Conference on Computer Vision (ICCV)*, pages 6532–6542.

Takatsuka, S., Miyamoto, N., Sato, H., Morino, Y., Kurita, Y., Yabuki, A., Chen, C., and Kawagucci, S. (2024). Millisecond-scale behaviours of plankton quantified in vitro and in situ using the event-based vision sensor. *Ecology and Evolution*, 14(8):e70150.

Tsilikas, I., Deligiannidis, S., Tsirigotis, A., Tsigaridas, G. N., Bogris, A., and Mesaritakis, C. (2023). Neuromorphic camera assisted high-flow imaging cytometry for particle classification. In *The European Conference on Lasers and Electro-Optics*, page ch_p_17. Optica Publishing Group.

Tsilikas, I., Tsirigotis, A., Sarantoglou, G., Deligiannidis, S., Bogris, A., Posch, C., Branden, G. V. d., and Mesaritakis, C. (2024). Photonic neuromorphic accelerators for event-based imaging flow cytometry. *arXiv preprint arXiv:2404.10564*.

Tsirigotis, A., Tsilikas, I., Sozos, K., Bogris, A., and Mesaritakis, C. (2023). Photonic neuromorphic accelerator combined with an event-based neuromorphic camera for high-speed object classification. In *European Quantum Electronics Conference*, page jsiii_3_4. Optica Publishing Group.

Vicente-Sola, A., Manna, D. L., Kirkland, P., Di Caterina, G., and Bihl, T. J. (2025). Spiking neural networks for event-based action recognition: A new task to understand their advantage. *Neurocomputing*, 611:128657.

Vinegoni, C., Feruglio, P. F., and Weissleder, R. (2018). High dynamic range fluorescence imaging. *IEEE Journal of Selected Topics in Quantum Electronics*, 25(1):1–7.

Vinegoni, C., Leon Swisher, C., Fumene Feruglio, P., Giedt, R., Rousso, D., Stapleton, S., and Weissleder, R. (2016). Real-time high dynamic range laser scanning microscopy. *Nature communications*, 7(1):11077.

von Erlach, T. C., Bertazzo, S., Wozniak, M. A., Horejs, C.-M., Maynard, S. A., Attwood, S., Robinson, B. K., Autefage, H., Kallepitis, C., del Río Hernández, A., et al. (2018). Cell-geometry-dependent changes in plasma membrane order direct stem cell signalling and fate. *Nature materials*, 17(3):237–242.

Wang, L., Ni, Q., Chen, C., and Yang, H. (2022). Lightweight target detection algorithm based on improved YOLOv4. *IET Image Processing*, 16(14):3805–3813.

Wang, S., Shan, X., Patel, U., Huang, X., Lu, J., Li, J., and Tao, N. (2010). Label-free imaging, detection, and mass measurement of single viruses by surface plasmon resonance. *Proceedings of the National Academy of Sciences*, 107(37):16028–16032.

Wilkerson, M. J. (2012). Principles and applications of flow cytometry and cell sorting in companion animal medicine. *Veterinary Clinics: Small Animal Practice*, 42(1):53–71.

Wojcik, K. and Dobrucki, J. W. (2008). Interaction of a dna intercalator draq5, and a minor groove binder syto17, with chromatin in live cells—influence on chromatin organization and histone—dna interactions. *Cytometry Part A: the journal of the International Society for Analytical Cytology*, 73(6):555–562.

Woo, S., Park, J., Lee, J.-Y., and Kweon, I. S. (2018). Cbam: Convolutional block attention module. In *Proceedings of the European Conference on Computer Vision (ECCV)*, pages 3–19.

Yamashita, R., Nishio, M., Do, R. K., and Togashi, K. (2018). Convolutional neural networks: An overview and application in radiology. *Insights into Imaging*, 9(4):611–629.

Yang, Z., Yang, L., Bao, W., Tao, L., Zeng, Y., Hu, D., Xiong, J., and Shang, D. (2022). High-speed object recognition based on a neuromorphic system. *Electronics*, 11(24):4179.

Young, Y. et al. (2021). Label-free white blood cell classification using refractive index tomography and deep learning. *BME frontiers*.

Zaouk, R., Park, B. Y., and Madou, M. J. (2006). Introduction to microfabrication techniques. *Microfluidic Techniques: Reviews and Protocols*, pages 5–15.

Zenker, J., White, M. D., Templin, R., Parton, R., Thorn-Seshold, O., Bissiere, S., and Plachta, N. (2017). A microtubule-organizing center directing intracellular transport in the early mouse embryo. *Science*, 357(6354):925–928.

Zhang, Z., Ma, M. S., Eshraghian, J. K., Vigolo, D., Yong, K.-T., and Kavehei, O. (2022). Work in progress: Neuromorphic cytometry, high-throughput event-based flow flow-imaging. In *8th IEEE International Conference on Event-Based Control, Communication, and Signal Processing (EBCCSP)*, pages 1–5. IEEE.

Zhang, Z., Xu, Z., Gu, X., and Xiong, J. (2024a). Cross-CBAM: A lightweight network for real-time scene segmentation. *Journal of Real-Time Image Processing*, 21(2):38.

Zhang, Z., Xu, Z., McGuire, H. M., Essam, C., Nicholson, A., Hamilton, T. J., Li, J., Eshraghian, J. K., Yong, K.-T., Vigolo, D., et al. (2023). Neuromorphic cytometry: Implementation on cell counting and size estimation. *Neuromorphic Computing and Engineering*, 3(4):044005.

Zhang, Z., Yang, H., Li, J., Chong, S. W., Eshraghian, J. K., Yong, K.-T., Vigolo, D., McGuire, H. M., and Kavehei, O. (2024b). Neuromorphic imaging cytometry on human blood cells. *bioRxiv*, pages 2024–11.

Zhu, L., Wang, X., Chang, Y., Li, J., Huang, T., and Tian, Y. (2022). Event-based video reconstruction via potential-assisted spiking neural network.

Zmijan, R., Jonnalagadda, U. S., Carugo, D., Kochi, Y., Lemm, E., Packham, G., Hill, M., and Glynne-Jones, P. (2015). High throughput imaging cytometer with acoustic focussing. *RSC Advances*, 5(101):83206–83216.